Air Force Institute of Technology

AFIT Scholar

3-26-2015

Verification and validation of Monte Carlo N-Particle 6 for Computing Gamma Protection Factors

William J. Erwin

Follow this and additional works at: https://scholar.afit.edu/etd

**VERIFICATION AND VALIDATION OF MONTE-CARLO N-PARTICLE 6
FOR COMPUTING GAMMA PROTECTION FACTORS**

THESIS

William J. Erwin, Captain, United States Army

AFIT-ENP-MS-15-M-090

DEPARTMENT OF THE AIR FORCE

AIR UNIVERSITY

AIR FORCE INSTITUTE OF TECHNOLOGY

Wright-Patterson Air Force Base, Ohio

AFIT-ENP-MS-15-M-090

VERIFICATION AND VALIDATION OF MONTE-CARLO NEUTRAL PARTICLE 6 FOR COMPUTING GAMMA PROTECTION FACTORS REPORT

Presented to the Faculty

Department of Engineering Physics

Graduate School of Engineering and Management

Air Force Institute of Technology

Air University

Air Education and Training Command

in Partial Fulfillment of the Requirements for the

Degree of Master of Science

William J. Erwin, BE

Captain, United States Army

12 January 2015

AFIT-ENP-MS-15-M-090

VERIFICATION AND VALIDATION OF MONTE-CARLO NEUTRAL PARTICLE 6 FOR COMPUTING GAMMA PROTECTION FACTORS

William J. Erwin, BE

Captain, United States Army

Committee Membership:

Dr. J. A. Clinton
Chair

Dr. J. W. McClory
Member

Maj B. J. Singleton
Member

AFIT-ENP-MS-15-M-090

Abstract

This thesis examined the suitability of a particle simulator known as "Monte Carlo n-Particle 6 (MCNP6) to determine how well U.S. Army vehicles shield their occupants from gamma radiation. MCNP6 compared favorably to three alternate modeling approaches and another particle simulator. In a validation experiment, MCNP6 was found to produce a gamma protection factor within 5% of the experimental result with 95% confidence. Further evaluations validated MCNP6's ability to produce reliable results with simplified or approximated inputs, model different sources, and position those sources in different shielding geometries. MCNP6 is suitable for evaluating gamma protection of Army vehicles and further research to explore the effects of different shielding shapes and evaluate the suitability for MCNP6 to calculate a comprehensive radiation protection factor is warranted.

This thesis is dedicated to the memory of

Anna

Acknowledgments

I thank God for giving me the gifts and the opportunity to study Nuclear Engineering here at AFIT. I consider it a great privilege to study and model the principles that govern His creation.

I thank my wife for her steadfast support throughout this endeavor. Her love has made me a better man, a better soldier, a better student, and a better father.

I thank Dr. Justin Clinton for his guidance through the process of conducting this research and writing this paper. His direction and counsel shaped my approach to this research.

I thank the members of my committee, as well as Dr. Kirk Matthews and Dr. James Petrosky, who provided valuable help throughout this process. Many of the topics I address in this paper were prompted by their suggestions.

Finally, I thank my colleagues and peers who helped me through classes and research in this degree program. Having such a helpful and supportive peer group has made this assignment the best of my career so far.

William J. Erwin

Contents

List of Figures

xiii

Tables

VERIFICATION AND VALIDATION OF MONTE-CARLO N-PARTICLE 6 FOR COMPUTING GAMMA PROTECTION FACTORS

1. Introduction

1.1. Motivation

How well does the United States Army's current fleet of combat vehicles protect soldiers from the unique effects of nuclear weapons? This simple question underscores a wide variety of tactical, operational, and strategic concerns. Exploding nuclear weapons emit powerful, invisible pulses of ionizing radiation in addition to their devastating thermal and blast effects. Unlike the blast and thermal effects, the ionizing radiation hazards persist long after the explosion in the form of radioactive fallout. Both the initial radiation pulse and the fallout can cause radiation sickness and death in the short term. In the long term, heavy doses of ionizing radiation can cause permanent health problems and many forms of cancer.

In order to manage these risks, the Army needs reliable and verifiable information on how well their vehicles protect crews and passengers from ionizing radiation. For planning purposes, this information is expressed as a radiation protection factor (RPF) that compares the expected radiation effects on an unshielded subject to the expected effects on a shielded subject in an otherwise identical radiation field.

1.2. Background

1.2.1. Past Methods of Experimental Evaluation

The most reliable method for evaluating this topic was demonstrated in the APPLE 2 test at the Nevada Test Site during OPERATION TEAPOT in 1955. Immediately after a 29 kT detonation atop a 500-foot tower, approximately 1000 soldiers in an armored task force called Task Force RAZOR drove to within 820 meters of the blast site as the mushroom cloud formed overhead. Upon reaching a threshold of 1 rad per hour inside the lead tanks, the task force turned and maneuvered to assault a designated nearby objective. Radiation monitors tracked exposures, both outside and inside the vehicles, as well as to all participating personnel [2].

While the APPLE 2 test conclusively proved that the 1955 fleet of vehicles could operate in the vicinity of a nuclear attack, it was never repeated. Although it is possible to extract some information about the radiation protection provided by the vehicles from the test data, Task Force RAZOR was intended to demonstrate capabilities and build confidence of a tactical formation, not to specifically evaluate the M48 tanks and M59 armored personnel carriers used. After the Partial Test Ban Treaty of 1963 precluded further tests of this nature, the Army developed several alternate methods for evaluating RPFs, which it used for the subsequent 30 years. These approaches included computational modeling, radioisotopes, and a high-energy X-ray facility.

As the U.S. Army fielded new vehicles during the Cold War, each chassis was tested and evaluated to address the threat of tactical nuclear weapons [3, 4, 15, 17, 18]. This testing evolved with improved computing power, more sophisticated modeling approaches, and better testing apparatus. The evaluations were designed to provide not

only a simple scalar RPF, but a comprehensive evaluation that would advise crews and leadership on how to position and configure their vehicles to maximize protection against known radiation threats [4,17,18].

Much of the early data driving gamma-based RPF assessments used radioisotopes with actual vehicles and radiation detectors [15]. These were often measured using single isotopes, most commonly ^{60}Co [16]. The complications of using constantly emitting, high-activity sources led to the development and use of the high-energy X-ray AURORA facility, which could activate or shut down its radiation upon command [8]. Although the still-active Gamma Irradiation Facility at Sandia National Laboratories was designed to accommodate an M1 tank, it has never done so.

After the Cold War ended, funding and interest in Army vehicle RPFs waned. The AURORA high-energy photon testing facility, which evaluated vehicle gamma protection factors (GPFs), ceased operation in 1994 [8]. An effort to conduct a prompt effects test on Army vehicles with a fast burst reactor was canceled due to a lack of funding. There is only one reactor currently available which can irradiate an Army vehicle with a prompt burst of fission radiation, the Fast Burst Reactor at White Sands Missile Range [16]. The last viable alternative for a prompt fission radiation burst was the Army Pulsed Radiation Facility, which was shut down in 2003 and demolished in 2010 [11].

1.2.2. Modeling Efforts

The first effort to model RPFs was the "Engineering Method" developed by the National Bureau of Standards. This method provided semi-empirical formulas for transporting gamma radiation through common materials and simple geometries [15].

3

Although this approach was useful for designing fallout shelters, it lacked the flexibility needed to model the complicated shapes and materials of a vehicle.

As computing technology improved, two new methods became viable: discrete ordinates transport codes and Monte Carlo methods. The discrete ordinates transport technique analytically solves the radiation transport problem in terms of the average particle with numeric integration techniques, whereas Monte Carlo methods use random sampling of individual particles to model the probabilistic nature of neutral particle interactions [2]. Monte Carlo methods emerged as the better modeling option in the 1980s. A crude discrete ordinates transport code is described in Chapter 3 and demonstrated in Chapter 5. Monte Carlo methods will be described in the Chapter 2 and discussed throughout the rest of this paper.

Although these efforts have been able to model parts of the radiation transport problem, the recent release of MCNP6 presents an opportunity to model all aspects of radiation transport in a single program. In response to a request from the United States Army Nuclear and Combating Weapons of Mass Destruction Agency (USANCA), and in coordination with the Defense Threat Reduction Agency (DTRA), a new research effort began in 2012. This effort's goal is to produce a method for generating reliable radiation protection factors for current Army vehicles [4, 14].

The first phase of this project was completed in the spring of 2014, when the neutron protection factor of a simple geometric surrogate, modeled using the Monte Carlo Neutral Particle 6 code (MCNP6), was experimentally validated. The simulation matched experimental measurements with a confidence level of 96% [4]. This investigation continued the same line of effort.

1.3.   *Purpose*

The goal of this work was to determine the suitability for MCNP6 as a model for determining gamma radiation protection factors for United States Army vehicles, using a simple geometric surrogate. This work included three supporting objectives. The first was to verify the suitability of MCNP6 by using other modeling approaches, such as discrete ordinates and simplified Monte Carlo methods. This verification included quantitative comparisons and qualitative evaluations.

The second objective was to validate MCNP6. The validation used a cubic, steel-walled enclosure with a 22×22×22 inch internal cavity as a surrogate for an Army vehicle. The validation compared experimental data from a detector inside and outside the enclosure to a simulation of the experiment in MCNP6. The threshold for successful validation was for the simulation to deliver a GPF that is within 5% of the experimentally-derived GPF with 95% confidence.

The final objective was to examine the influence of different factors on the modeled and experimental GPFs. These factors included using different photon energies, different geometric configurations, variance reduction techniques, spectral analysis and processing techniques, and different model fidelities. This objective was a broad effort that included physical experimentation, modeling, and data processing techniques in order to analyze these influences and suggest good practices for future research.

2. Theory

This chapter discusses the theory of gamma radiation transport that supports this research, methods for computing dose and radiation protection factors, the theory behind Monte Carlo methods, information about MCNP6, and an overview of alternate models.

2.1. High-Energy Photon Interactions with Matter

Individual high-energy photons may interact in several ways with matter. The location and type of interaction are driven by probabilities known as cross sections. There are two categories of cross sections: microscopic and macroscopic.

A microscopic cross section describes the probability of interaction associated with a single atom. This term is essential for determining the mean free path, or average distance to an interaction for photons of a given energy. A macroscopic cross section sums up these probabilities for all types of atoms in a material. In mathematical terms [6],

$$\Sigma_{\mathrm{x}} = \sum_{\mathrm{i}=1}^{\mathrm{n}} (\sigma_{\mathrm{i}} \rho_{\mathrm{i}}), \tag{1}$$

where Σ_{x} is the macroscopic cross section, σ_{i} is the microscopic cross section of an atom, ρ_{i} is the density of atoms of that type in the material, and n is the number of different isotopes in the material.

The microscopic cross section can be further broken down into types of interactions. Gamma rays tend to interact with matter through three well-understood mechanisms: photoelectric absorption, pair production, and Compton scattering [5,6]. The total microscopic cross section is a simple summation of the microscopic cross sections of each type of interaction, or [6]

6

$$\sigma_{\mathrm{tot}} = \sigma_{\mathrm{pp}} + \sigma_{\mathrm{pe}} + \sigma_{\mathrm{cs}}, \tag{2}$$

where σ_{tot} is the total microscopic cross section, σ_{pp} is the microscopic cross section for pair production, σ_{pe} is the microscopic cross section for photoelectric absorption, and σ_{cs} is the microscopic cross section for Compton scattering. The microscopic cross sections of these interactions depend upon the number of protons in the material and the energy of the interacting photon, as show in Figure 1.
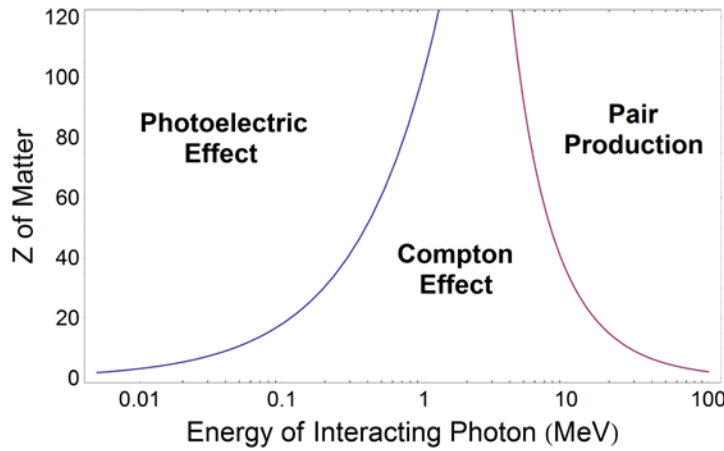
Figure 1. This chart shows the dominant regions of each type of interaction based upon the number of protons (Z) in the material and the energy of the incident photon. The lines approximate values at which neighboring interaction regions are equally likely [5].

In photoelectric absorption, a photon interacts with an absorbing atom. Some of the energy of the photon overcomes the binding energy of one of the atom's electrons, which releases that electron. The rest of the interacting photon's energy provides the released electron with kinetic energy. Since charged particles have mean free paths far shorter than that of equivalent-energy photons [7], secondary electrons from this interaction are unlikely to travel through an armor plate. Thus, unless the photoelectric

absorption happens at or near an inner surface of a shield, it is unlikely to transport much energy beyond the shield.

In a pair production event, a high-energy photon interacts with an atom's nucleus and produces two beta particles of opposite charge. In order to balance the energy of this interaction, the incident particle must have energy greater than or equal to the summed mass energies of both beta particles. Figure 1 shows that, for the heaviest elements, pair production becomes a dominant interaction mechanism for photons with energies over approximately 5 MeV. Since iron has 26 protons per atom, pair production becomes a dominant interaction at 10 MeV, which is far more energy than nearly every photon produced in a nuclear weapon explosion [2]. Since the Army's interest in this program is driven by the unique effects of nuclear weapons, there is little need to evaluate photons with energies at and above 10 MeV.

Compton scattering is the primary interaction of interest for this work. In a Compton interaction, a photon interacts with an electron and deflects, imparting some of its energy to the electron. In an iron barrier, the electron's mean free path is so short as to make its effects negligible for interactions that are not at or near the inner surface of the barrier [7], but the photon is much more likely to continue through the iron barrier without further interactions. The amount of deflection that the photon experiences is a probabilistic outcome described by the well-known Klein-Nishina distribution [5,6],

$$\frac{\mathrm{d}\sigma}{\mathrm{d}\Omega} = \frac{\alpha^2 r_c^2 P\left(E_\gamma, \theta\right)^2 \left[P\left(E_\gamma, \theta\right) + P\left(E_\gamma, \theta\right)^{-1} - 1 + \cos^2\left(\theta\right)\right]}{2},\qquad(3)$$

where α is the fine structure constant, $\dfrac{d\sigma}{d\Omega}$ is the solid angle cross section, and $P\left(E_\gamma, \theta\right)$

is the ratio of input and output photon energies given by the Compton scattering equation
[5,6],

$$P\left(E_\gamma, \theta\right) = \frac{1}{1 + \left(E_\gamma \middle/ m_e c^2\right)\left(1 - \cos\theta\right)},\tag{4}$$

where E_γ is the energy of the incident photon and θ is the scattering angle. The energy

dependence of the distribution is demonstrated in Figure 2 for a few sampled energies.

Since most of the photons of interest have energies between 100 keV and 4 MeV, the

scattering angles will tend to be small, so that the scattered photon leaving the interaction

will have most of the energy of the incident photon.
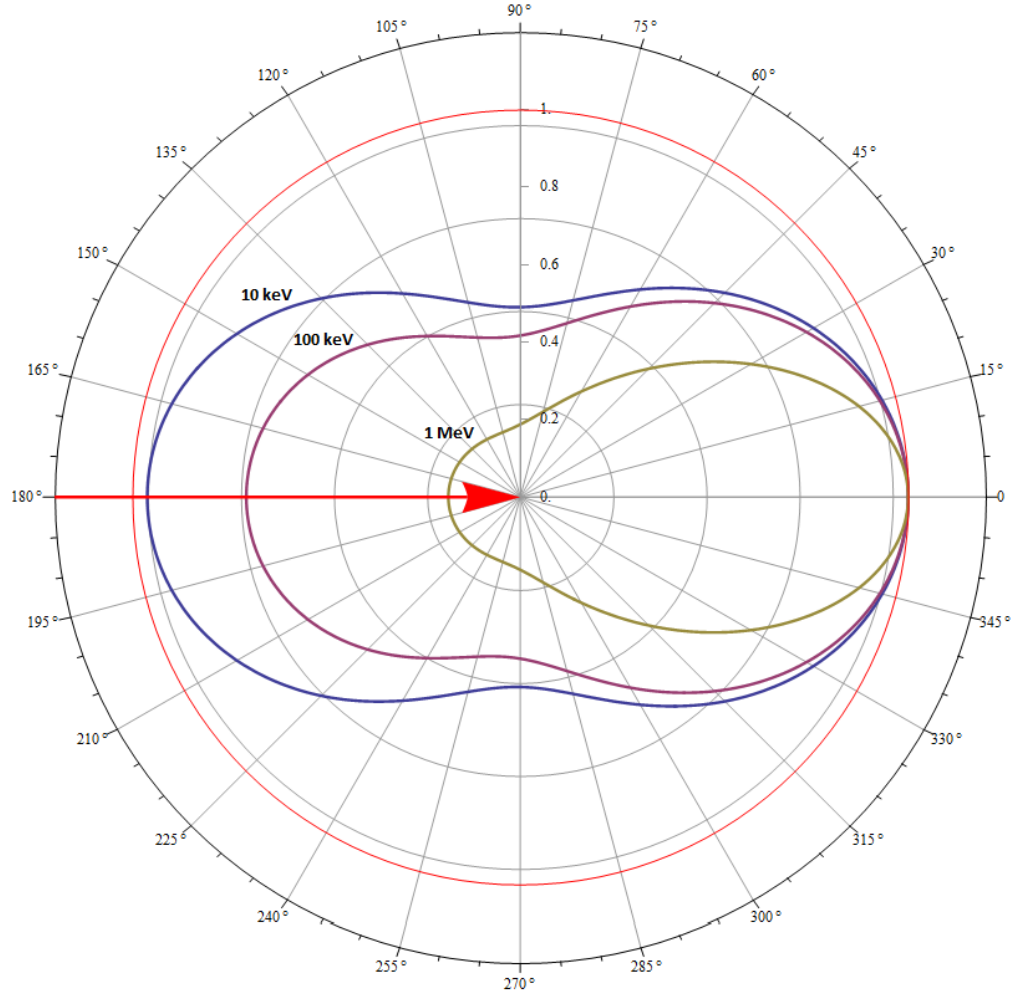
Figure 2. Polar plot of Klein Nishina distributions at 10 keV, 100 keV, and 1 MeV [13].

2.2. *Gamma Protection Factor*

In its simplest form, a radiation protection factor (RPF) is a ratio comparing the effects of ionizing radiation in a protected state to the effects of ionizing radiation in an unprotected state [14, 15],

$$\text{RPF} = \frac{\text{Free Field Dose}}{\text{Shielded Dose}}. \tag{5}$$

Since charged-particle radiation at energies associated with nuclear weapons does not have any significant ability to penetrate solid matter [5], this generalized RPF can ignore the influence of alpha and beta radiation as external sources. However, it is important to note that photons which Compton scatter, or interact by photoelectric absorption, at or near the inner surface of the iron barrier may release energetic electrons that subsequently contribute to the dose of vehicle occupants as a secondary source of ionizing radiation. If these electrons transport significant amounts of radiation out of the barrier, then they will create bremsstrahlung radiation and increase the low-energy photons measured in experimental observations above what is predicted by a model that does not include these secondary electrons. Either way, these electrons are a secondary product of gamma or neutron radiation, so the RPF formula can therefore be broken down into a sum of a neutron and a gamma protection factor [4,14,15],

$$\mathrm{RPF} = \mathrm{NPF} + \mathrm{GPF}, \tag{6}$$

where

$$\mathrm{NPF} = \frac{\mathrm{FreeFieldNeutronDose}}{\mathrm{ShieldedNeutronDose}}, \tag{7}$$

and

$$\mathrm{GPF} = \frac{\mathrm{FreeFieldGammaDose}}{\mathrm{ShieldedGammaDose}}, \tag{8}$$

where GPF is the gamma protection factor and NPF is the neutron protection factor. How then, should we define the free field and shielded gamma doses? In general, there are three approaches: exposure, dose, and dose equivalent.

11

Exposure is defined by the charge created within a mass of air by photon radiation and is measured in Roentgens (R), which are defined as $1\mathrm{R} = 2.58 * 10^{-4} \mathrm{C}\!\!\Big/\!\!_{\mathrm{kg}}$. This unit of exposure is often used in the study of radiation protection [5]. However, this depends on cross section data for air, and therefore must be adjusted to reflect the differences in density and cross section between air and a target material of interest, such as soft tissue. The exposure rate can be computed using discrete intervals of a full spectrum, using [10]

$$\dot{\mathrm{X}}[\mathrm{E}_{\mathrm{photons}}] = \frac{\phi\left(\dfrac{\mathrm{ph}}{\mathrm{cm}^2 * \mathrm{s}}\right) * \mathrm{E}_{\mathrm{photons}}\left(\mathrm{MeV}\right) * 1.6 * 10^{-13}\left(\dfrac{\mathrm{J}}{\mathrm{MeV}}\right)\mu_{\mathrm{air}}\left(\dfrac{1}{\mathrm{cm}}\right)}{\rho_{\mathrm{air}}\left(\dfrac{\mathrm{kg}}{\mathrm{cm}^3}\right) * 34\left(\dfrac{\mathrm{J}\big/\mathrm{kg}}{\mathrm{C}\big/\mathrm{kg}}\right)}, \quad (9)$$

where $\dot{\mathrm{X}}[\mathrm{E}_{\mathrm{photons}}]$ is the photon-energy-dependent exposure rate associated with a monoenergetic flux, ϕ is the flux of the photons, ph is a number of photons, $\mathrm{E}_{\mathrm{photons}}$ is the energy of the photons, μ_{air} is the cross section associated with photons of that energy in air, and ρ_{air} is the density of air. In order to convert the exposure rate into a dose rate, we use [10],

$$\dot{\mathrm{D}}[\mathrm{E}_{\mathrm{photons}}] = \dot{\mathrm{X}}[\mathrm{E}_{\mathrm{photons}}] \times 34 \times \frac{\mu_{\mathrm{mat}}\big/\rho_{\mathrm{mat}}}{\mu_{\mathrm{air}}\big/\rho_{\mathrm{air}}}, \quad (10)$$

where $\dot{\mathrm{D}}[\mathrm{E}_{\mathrm{photons}}]$ is the dose rate in units of gray per second. Conversions must be done in discrete energies, so this method is typically applied with exposure rate constants for

the characteristic energies of specific radioisotopes [5,9]. Given that both prompt and delayed effects of nuclear weapons emit broad spectra of high-energy photons [2], and given that MCNP6 does not have a tally mechanism for exposure, this approach can be challenging to simulate, especially for high-resolution simulations with large numbers of bins.

Another method is to evaluate the absorbed dose for a protected body against the absorbed dose for an unprotected body. Dose measures the total energy deposited per unit mass, and it is measured in units of gray (Gy) and rad, defined as $100 \text{ rad} = 1 \text{ Gy} = 1 \text{ J}/\text{kg}$ [2,5,6]. Dose depends upon a wide variety of variables, including the geometry of the object of study. Since human bodies inside vehicles may come in a wide variety of sizes and poses, and since detectors tend to have different cross sections than human tissues, a sound method for evaluating GPFs is to first validate MCNP6 by dose depositions in experimental and simulated detectors. With this validation complete, MCNP6 can then simulate the dose deposited in a volume of surrogate material to produce a reliable human body-based GPF.

Another approach is to compare kerma to protected and unprotected targets. Kerma refers to the total kinetic energy deposited by ionizing radiation per unit mass [5,6,9]. Although it is given in the same units as dose, kerma tends to be higher than the actual energy imparted to a material. Some of the energy imparted is subsequently released by Bremsstrahlung radiation, which can escape from the volume of interest [5,6,9]. This feature may make it a good choice for a worst-case evaluation of a body or

object in MCNP6, but it is difficult to evaluate experimentally, since all secondary electrons must be captured.

2.3.   *Other Considerations*

Some types of ionizing radiation have more adverse health effects than others due to high coefficients of linear energy transfer. This is particularly true of heavy charged particles [9]. For high-energy photons, however, this is not a significant factor, since the International Commission on Radiation Protection (ICRP) recommends that all energies of photons be assigned a weighting factor of 1, the lowest weighting factor [5].

Although the primary penetrating form of ionizing radiation for this study is the high-energy photon, these photons deposit their energies by creating, releasing, and exciting electrons. Although the iron shielding is likely to stop most of these electrons due to their low mean free path in iron, any electrons released or excited at or near the inner surface of the iron box may contribute a significant amount of ionizing flux to the shielded environment. The ICRP recommends that electron radiation be assigned a weighting factor of 1 [5].

Modern Army vehicles use far more electronics than their Cold War era counterparts. This introduces the question of how vulnerable the vehicles' systems are to ionizing radiation. This may be a valid question in the future, but most modern commercial electronics require 50 Gy or higher to show significant degradation, which is approximately 25 lethal doses [10].

2.4. Monte Carlo Methods

A Monte Carlo approach to modeling particle transport produces an approximation of actual data by tracking individual particles. It accomplishes this through the arrangement of virtual geometric configurations of materials to produce statistically significant results.

This approach begins by randomly sampling an energy, direction, and distance a particle will travel until it interacts. The energy depends on the source used. The direction is a random sampling of an even distribution of angles. The distance to an interaction can be sampled by the equation

$$dis \tan ce = \frac{-\ln(\text{Rand}(0,1))}{\ln(2)},\qquad(11)$$

where Rand(0,1) is a random real number between 0 and 1 [1]. This produces a probability distribution such that half of the sampled interaction distance is between one and zero, and half is between one and infinity.

The next step in the Monte Carlo process is to transport the particle in its trajectory until it reaches its interaction distance. This depends on the particle's mean free path length in whatever medium it happens to pass. The mean free path length is determined by the particle's energy, as well as the medium's density and experimentally derived attenuation data [1].

If the particle crosses into a new material before its interaction distance is exhausted, a new interaction distance is determined. Otherwise, the particle interacts. The type and outcome of the interaction are energy-dependent; see section 2.1 for more information. Secondary particles are generated from this interaction, and these particles are tracked by this same methodology until they meet kill criteria, either by exiting the

volume of interest or by losing so much energy that they are no longer a significant source of ionization [1].

2.5.   *Monte Carlo n-Particle Code 6 (MCNP6)*

Developed by Los Alamos National Laboratories, MCNP6 was released in 2013 [1]. As the successor to a series of programs dating back to the first Monte Carlo modeling efforts in the 1940s, MCNP6 has a number of useful features that go far beyond neutral particles to include 36 types of particles and an enormous library of interaction mechanisms and cross sections [1]. Its predecessors, MCNP5 and MCNPX, used Monte Carlo methods to simulate different types of particles, and were developed in parallel as separate simulation packages. MCNP5 could not transport charged particles, while MCNPX could not transport neutral particles. MCNP6 merged the capabilities of both programs into a single simulation platform.

User inputted text files drive MCNP6 in a series of lines known as 'cards.' The first are the cell cards, which describe the geometric spaces within the simulation, their densities, and how they are positioned. The second are the surface cards, which describe the cell boundaries. Material data cards define the proportions of elements and isotopes in each cell. Other data cards specify the particles of interest, source information, types of tallies, bin structure, criticality codes, variance reduction techniques, and many other options [1]. Examples of MCNP6 input files are in Appendix B.

2.6. *Potential Sources of Error*

Even with the right input file, MCNP6 does not account for dead time in a detector, the relative efficiency of a detector, or the response function associated with a detector. Additionally, if the input deck of MCNP6 is not configured to track electrons, it may ignore a significant source of dose within a protected region.

The dead time in a detector is highly dependent upon the type of detector and the electronic system associated with that detector. The Nyquist criterion requires a sampling rate twice that of the measured signal in order to resolve the signal. If the system cannot sample fast enough to establish the Nyquist rate for two or more photons, then the system fails to record the extra photons [5]. This is a significant concern when using the same source and detector in both a shielded and unshielded configuration. An unshielded configuration with a strong enough source could lead to saturation effects, which would degrade the utility of the data by making the unshielded activity appear lower than it is. Timing the response function and multiplying it by the number of counts recorded in a given operation can yield the total dead time for a particular run. Subtracting the dead time from the measurement time determines a more reliable interaction rate.

Another potential source of error is electronic system noise. If the signal-to-noise ratio is not sufficiently high, then data is lost in the random fluctuations of the system. This could be a significant problem for low-activity scenarios such as a detector surrounded by the iron box as in this work.

No detector is perfect, and a flux of monoenergetic photons into a spectroscopic instrument will register as a sloped peak, not a single-bin line. This detector response is

an inherent function of electronic noise, power fluctuations and the experimental tolerance of the associated components. Since MCNP6 tracks actual particle behavior, it will put all particles of a monoenergetic flux into a single energy bin. Thus, the detector response must be emulated if one wishes to use MCNP6 to predict actual detector spectra. The full width and half maximum of a signal shows the difference between the independent variable at half the maximum height of the dependent variable [5]. By measuring the full-width at half-max of a known peak, it is possible to synthesize a point spread function which, when convoluted with a MCNP6 generated spectrum, yields a prediction of actual experimental data.

Electrons released from the barrier or the air within a shielded enclosure may pose another issue. Compton interactions are the primary absorption mechanism of interest for transport in this work, but all three types of high-energy photon interactions can release electrons from the inner surface of the iron box. Although these electrons are not as penetrating as the down-scattered photons, they may contribute to dose.

2.7. *Hypothesis Testing and Confidence Intervals*

This work used a null hypothesis evaluation to determine if the GPF produced by MCNP6 was or was not valid. The initial research hypothesis of this thesis was that an MCNP6 model of a shielded and unshielded detector subjected to the same external radiation produces a GPF within 5% of the GPF determined by real experiments of the same configuration. This can be stated in mathematical terms as

$$\left| \mathrm{Modeled GPF} - \mathrm{Real GPF} \right| \leq .05 * \mathrm{Real GPF}. \tag{12}$$

The null hypothesis of this experiment is that the MCNP6 model of a shielded and unshielded detector subjected to the same external radiation produces a GPF that is more than 5% different from the corresponding GPF determined by real experiments of the same configuration. This can be stated in mathematical terms as

$$\left| \mathrm{ModeledGPF} - \mathrm{RealGPF} \right| \geq .05 * \mathrm{RealGPF}. \tag{13}$$

MCNP6 output files provide the variance of a tallied dose; taking the square root of this variance yields the value of its standard distribution. Assuming that the GPF is normally distributed, and enough points are sampled by both the experiment and the simulation, a two-tailed test with a p-value of 0.05 should disprove either the hypothesis or the null hypothesis [11].

3. Experimental Methods and Modeling

This chapter describes the setup and execution of experiments and modeling simulations to verify and validate MCNP6 as a model for producing GPFs. It also explores evaluation techniques and alternate experimental configurations for investigating GPFs.

3.1 Overview of the Plan

For the work's first objective of verifying MCNP6 as a suitable choice for modeling gamma transport, four alternate models were compared to MCNP6 results. The alternate models fell into two categories: non-Monte Carlo techniques and Monte Carlo techniques. In an effort to include alternate programming languages, these alternatives were written on different programming platforms. All told, this work attempted to model photon transport in Mathematica, MATLAB, GEANT4 (in C++), and MCNP6, which is written in FORTRAN. The relative merits of the programming languages are not addressed; rather, the overall processing time, portability, versatility, and features provided a basis for evaluating and comparing the techniques.

The second objective of validating GPFs produced by MCNP6 consisted of a simple experiment in which a single-peak source irradiated a detector in a simple cubic steel enclosure and in a free field environment. The experiment was run twice, once with a NaI detector, and once with a HPGe detector.

The final objective of evaluating the parameters behind GPF validation consisted of several series of simulations and experiments. The first series substituted three different sources to establish the range of energies that could be validated. The second

was a series of simulations investigating the importance of geometric fidelity, material data fidelity, and track counts to achieving validation. The third series investigated MCNP6's ability to produce valid GPFs for thicker and more-complicated shielding geometries.

3.2 Verifying MCNP6 vs Non-Monte Carlo Methods

This section describes the methodologies used to evaluate non-Monte Carlo photon transport techniques against MCNP6. Two models were constructed and evaluated: attenuation and quadrature.

3.2.1 Verifying MCNP6 vs Attenuation

Although analytical methods could not model the precise behavior of photon transport above the quantum scale, it was possible to model some simpler aspects of photon transport with a single equation: the exponential attenuation of a monoenergetic photon beam. Figure 3 is a representation of the scenario modeled. This model made many simplifying assumptions, such as directing all photons on a perpendicular path through an iron barrier of finite thickness but infinite width and height.

For this work, the model was constructed in Mathematica to provide a fast and reliable analytical check of MCNP6 peak photon transport. The governing equation for monoenergetic photon attenuation in matter is

$$F = F_0 e^{-\mu \rho x}, \tag{14}$$

where F is the flux of a stream of monoenergetic photons at a given depth in a barrier x, F_0 is the original flux before entering the barrier, μ is the microscopic cross section for a photon of that energy in that material, and ρ is the density of the material [6].
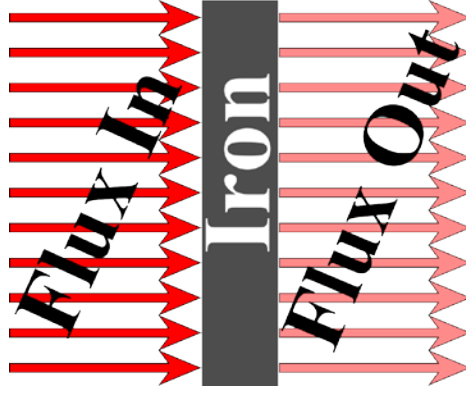
Figure 3. Diagram of the Mathematica model, with uniform flux into and out of an iron barrier.

The cross section μ depends on both the materials and the energy of the photons, and is provided in material data tables by the National Institute of Standards and Technology (NIST) [7]. Since most photon energies cannot be expected to have the exact reference energies in these tables, the cross sections must be interpolated using log-log interpolation.

This analytical model can be directly compared to MCNP6 by running two simulations with a monoenergetic source and a detector: one with an iron barrier between them, and one without. The ratio of the peak energies deposited in the detector should coincide with the ratio of the analytical model's attenuated peak photons to the original flux.

$$\frac{\phi_{\text{in}}\left(\text{analytical}\right)}{\phi_{\text{atten}}\left(\text{analytical}\right)} = \frac{\phi_{\text{Bare}}\left(\text{MCNP6}\right)}{\phi_{\text{Shielded}}\left(\text{MCNP6}\right)}, \tag{15}$$

where ϕ_{in} is the flux going into the shield in the simple attenuation model, ϕ_{atten} is the attenuated flux coming out of the other side of the shield in the simple attenuation model, ϕ_{Bare} is the flux going into the surface of the unshielded detector, and $\phi_{Shielded}$ is the flux going into the surface of the shielded detector.

3.2.2 Verifying MCNP6 vs a Quadrature Model

Although the analytical model provides reliable and verifiable results for monoenergetic photon penetration and attenuation, it does not provide information about scattered photons. The Mathematica model from the previous subsection was expanded to demonstrate this behavior for two successive Compton scatter events. This approach used numerical integration (or quadrature) techniques by breaking up all probabilistic components of an interaction into discrete groups, sub-groups, and sub-sub-groups as the model progresses through one and two subsequent Compton scatterings. Although crude by modern standards, this is the essence of how discrete ordinates codes work.

All interactions are sampled in discrete increments of a single degree, with normalized weighting depending on that angle's probability as determined by the Klein-Nishina distribution (See Figure 2 in the previous chapter).

For the purposes of this model, all photons that are attenuated in the previous section are assumed to Compton scatter at a distance of one mean free path into the barrier. Since the photons going into this first Compton scattering are all normal to the plane of the barrier, photons with the same scattering angle all have identical path lengths through the rest of the iron barrier. These photons must then be attenuated along these

path lengths to produce a spectrum of photons that scatter forward once and pass through the rest of the iron barrier.

Further Compton interactions follow a similar logic to the first; all attenuated photons from the first scattering are assumed to scatter again at a distance of one mean free path further into the iron. However, this introduces an additional complicating factor, in that these photons are no longer moving normal to the plane of the barrier. Thus the scattering angle from this second interaction must be revolved about the axis of the inbound photon to this second interaction. In addition to further dividing the photons into 180 scattering angle groups, these angles must be divided into another 360 angles of revolution.

The angles of the inbound photon, the incremental scattering, and the revolution of that scattering about the axis of the inbound photon produce a new angle with respect to the normal vector of the barrier plane. This is done through the Law of Cosines for Spherical Triangles [12],
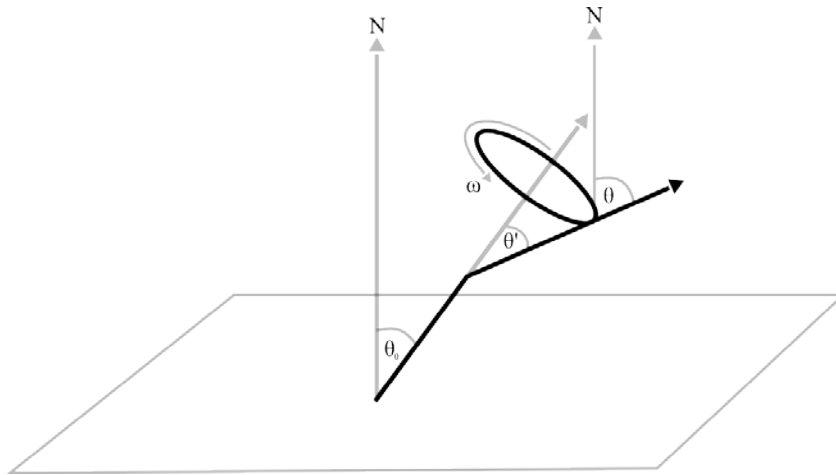
Figure 4. A representation of a Compton interaction. N is an arbitrary reference vector, which is aligned with the axis of the iron barrier for the slab geometry of the Mathematica and MATLAB simulations.

$$\mathrm{Cos}\left(\theta\right) = \mathrm{Cos}\left(\theta'\right)\mathrm{Cos}\left(\theta_0\right) + \mathrm{Cos}\left(\omega\right)\mathrm{Sin}\left(\theta_0\right)\mathrm{Sin}\left(\theta'\right), \qquad (16)$$

where θ is the angle of the scattered photon with respect to the normal vector of the barrier plane, θ' is the input angle with respect to the normal vector of the barrier plane, θ_0 is the scattering angle of the Compton interaction, and ω is the angle of rotation applied to the scattered angle about the vector of the inbound photon. Figure 4 is a representation of the angles involved.

The resulting model should, given enough interactions, provide a rough approximation for the expected flux of a photon stream through an iron barrier. Of particular interest is the number of subsequent Compton scatterings that this approach can practically model.

The results of this model were compared to a MCNP6 model using both quantitative and qualitative criteria. The quantitative criteria included processing time and file sizes. Although this model produced spectra, they were compared to MCNP6 spectra in terms of the spectra's shape and features, not the counts associated with those features. The qualitative criteria included a subjective assessment of the flexibility of this technique, the complexity of writing an input file, and the applicability of this approach to the problem.

3.3 Verifying MCNP6 vs Other Monte Carlo Programs

This section describes two alternate Monte Carlo programs and how they were configured to solve the same problem as MCNP6. The first program was a custom MATLAB script. The second was a GEANT4 simulation.

3.3.1 Slab Geometry Monte Carlo Model in MATLAB

The purpose of this subsection of the work is to develop a Monte Carlo script in MATLAB that models photon transport through a barrier of finite thickness but infinite height and width, the same geometric assumptions as the previous section's Mathematica model. Unlike that model, however, each photon was tracked individually by randomly sampling the interaction distributions through as many Compton interactions as it took to meet a kill criteria. Photons tracks began at a point source and ended either by passing out of the volume of interest or losing too much energy to be of further interest.

Figure 5. MATLAB monte carlo model slab diagram.

Figure 5 shows a representation of the MATLAB Monte Carlo script's geometry. The slab geometry thicknesses used in the MATLAB model closely matched the linear

dimensions of the baseline experimental setup along a ray going out from the source through the center of the NaI detector in the center of the iron box. This was modeled as a plane source, a slab of air, a slab of iron, a slab of air, and a plane representing the surface of the NaI. The result was an energy spectrum of photon energies crossing into the NaI, which could then be multiplied by the appropriate geometric and dose conversions to approximate the spectrum of energies deposited for the MCNP6 model.

3.3.2 GEANT4 Model

This section describes how GEANT4 was applied with an identical setup to MCNP6. GEANT4 is an open-source Monte Carlo simulation program originally developed by CERN. While it has similar simulation capabilities to MCNP6, GEANT4 is written in C++ and requires the user to write considerably more code to define a simulation.

The models were set up to simulate the planned validation experiment described in the next section. Both simulations consisted of identical iron boxes with air inside and outside, as well as identical NaI detector cylinders placed in the middle of the boxes. Both simulations ran 662 keV gamma rays from isotropic point sources at the same relative positions outside the steel boxes for an identical number of tracks; these were meant to simulate a radioisotope sample of ^{137}Cs. The energies deposited within the NaI detectors were reported as histograms with the same number of bins.

Output spectra from the custom MATLAB program, GEANT4, and MCNP6 were compared by qualitative and quantitative criteria. The quantitative criteria included a direct comparison of photon energy spectra deposited in the NaI detectors, processing

time, relative peak heights, and file sizes. The qualitative criteria included program flexibility, input file complexity, portability, and adaptability to different aspects of a GPF investigation.

3.4 Validating MCNP6 in a Simple Experiment

Although establishing validation was the second supporting objective of this work, it was the most important. This primary experiment compared the shielded and unshielded spectra and dose rates of two detectors subjected to the same radioactive source at the same distance. The experiment was designed to be as simple for MCNP6 to model as possible. Later work would evaluate more complicated scenarios to challenge MCNP6 and explore the limits of evaluation.
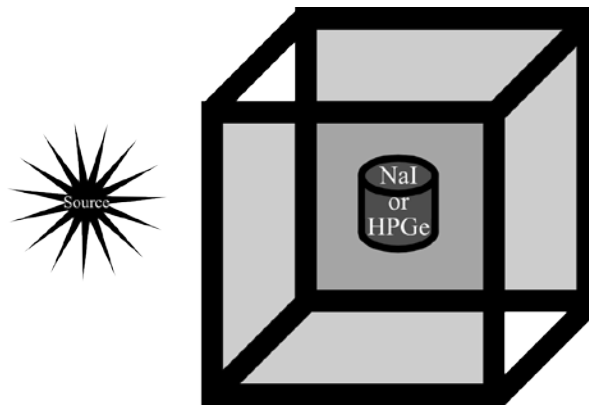
Figure 6. Simple diagram of a shielded observation, not to scale.

3.4.1 Experimental Equipment and Setup

The test enclosure consisted of a cubic aluminum frame with an assortment of 18 steel plates which could be bolted onto the frame to form a shielding barrier. Each member of the aluminum frame had a 2 inch by 2 inch cross section and outer edges 22

inches long. Inside the enclosure, a light aluminum scissor jack held the detector such that the detection crystal was centered in the middle of the enclosed space, 11 inches from all faces. Figure 7 shows the frame with the jack and stand in their relative positions.
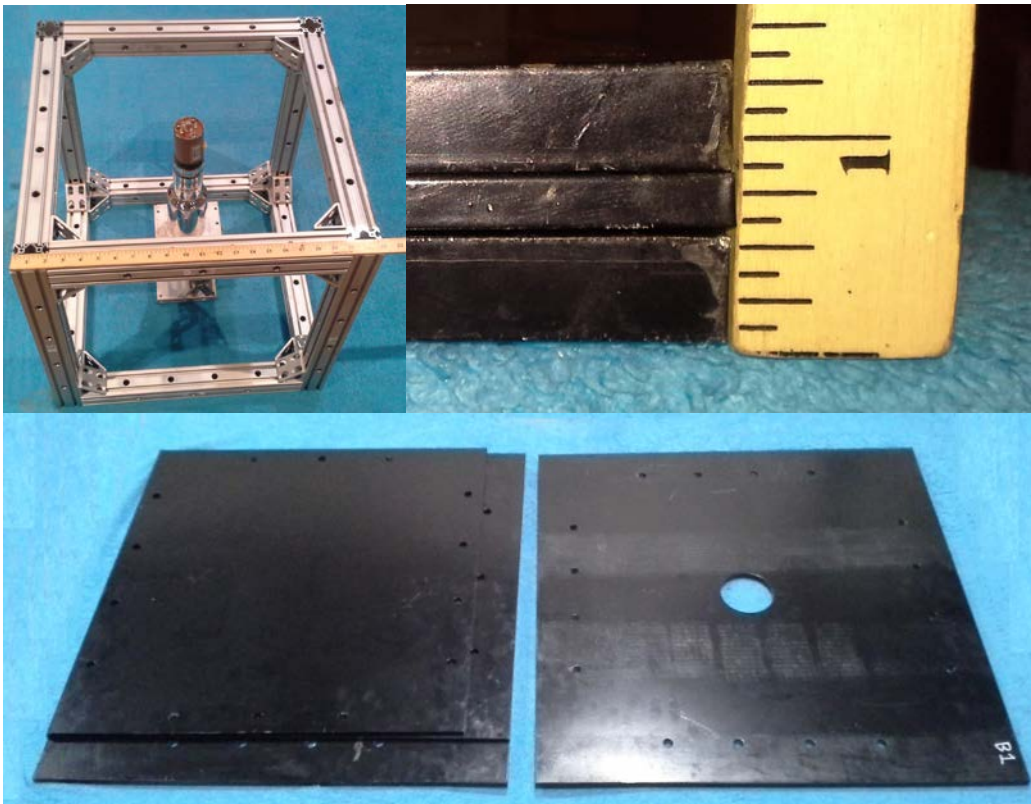
Figure 7. The enclosure's components. Top left shows the frame with the stand and detector inside. Top right shows the thicknesses of the plates. Bottom shows the various plates; note their differences in length and width.

The plates themselves were made in sets of three for each face of the enclosure. Two plates of each set had thicknesses of ½ inch, while the third had a thickness of ¼ inch. They were cut to form a cubic shape when all 18 plates were bolted onto the aluminum frame. For the initial validation experiment, only the ¼ inch plates were used. In this thinner assembly, the plates overlapped at the edges and corners, as shown in

Figure 8. The source was therefore placed in a face-centered position, 3 inches away from the inner surface of the near steel plate.

Figure 8. Scale model of the assembled enclosure with only the ¼ inch plates on (left) and all three plates on (center), and the source placement for the initial validation experiment (right).

The NaI detection system was set up according to Figure 9. The NaI detector was a Saint-Gobain model 3M3/3 with an ORTEC model 226 photomultiplier tube base. The preamplifier was an ORTEC model 113. The EG&G ORTEC DART was a multi-role component, as it both provided the high-voltage power supply and served to amplify and digitize the signal. Gammavision allowed the desktop computer to control data collection, display it in real time, and output it into spectra files for subsequent data processing.
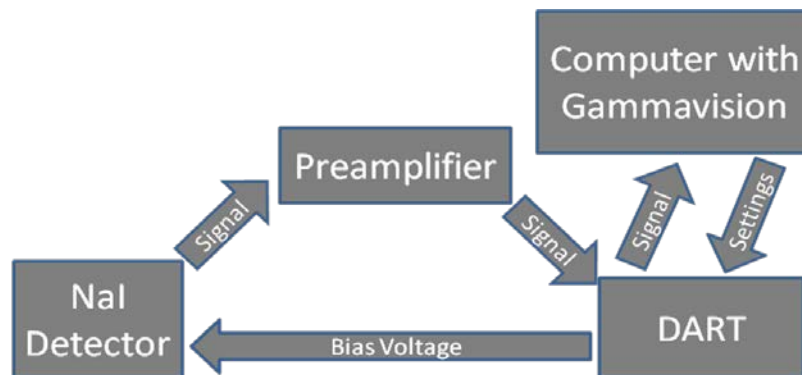
Figure 9. Diagram of experimental setup for NaI detector system.

The Gammavision settings for the Dart were established in early calibrations and retained throughout the rest of the work. The high voltage power supply was set to 900 V. The TTL was in shutdown mode. The ADC gate was off, its conversion gain was set to 8192 bins to allow maximum resolution, and the lower level discriminator was set to 88. The energy calibration in Gammavision was established by assigning a value of 662 keV to the center bin of the observed peak and applying a simple linear equation going through the origin of the spectrum.

The HPGe detector system setup was similar in most respects to the NaI detector system setup. The most significant difference was the inclusion of a cryogenic Sterling cooling system. This consisted of an ORTEC Cryosecure Compressor™ Power Controller, an ORTEC X-Cooler™ II, and an ORTEC Pop Top Model GEM-50195-P-LP. Figure 10 shows the setup configuration scheme and the detector.
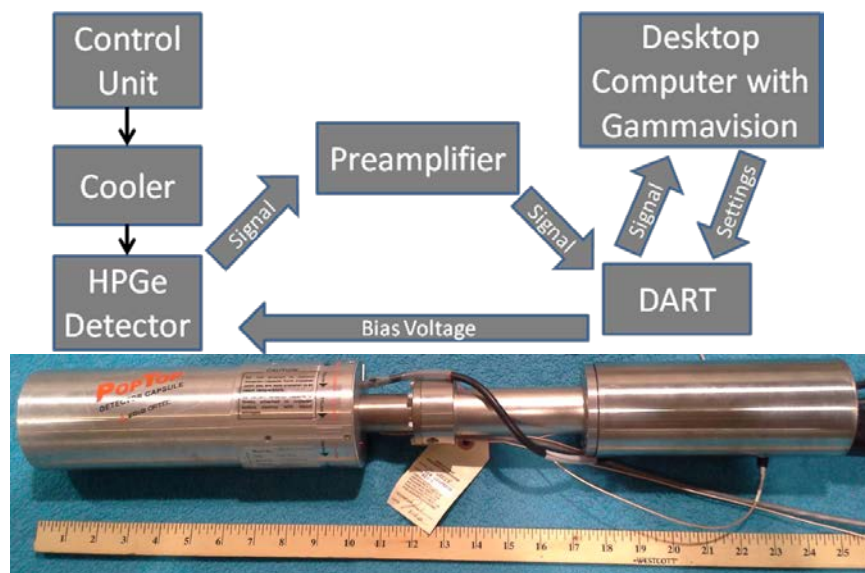
Figure 10. HPGe Detector System Diagram and picture of the detector.

The HPGe detector was slightly larger than the opening in the enclosure's top plate. For the initial validation, the top panel was removed to avoid the necessity of disassembling and reassembling the detector. Since the detector had a 3-day cooldown and warm-up time, this presented potential delay for later experimental observations. However, this became unnecessary, as the HPGe was not used after the initial validation experiment for reasons discussed in Section 5.4.

^{137}Cs was selected as the source for the initial experiment due to its single 662 keV photon emission peak. Simulations in the previous sections indicated that ^{137}Cs would penetrate the steel in significant quantities for its maximum peak and in its downscattered regions. The source was placed 3 inches outside the inner surface of the steel barrier, or 2 ¾ inches from the outer surface. After taking a shielded observation, the detector and stand were removed from the enclosure and placed on a nearby table. With the source 14 inches away and at the same height as the detector crystal's center, another observation was taken.

Rather than setting a fixed observation time, the end of an observation was driven by a subjective assessment of whether or not the key features of a spectrum had resolved with an acceptable signal-to-noise ratio. The spectra produced were normalized to their observation times in later data processing in MATLAB, which summed the weighted dose contributions of each bin to produce a single dose value. Dividing the free field dose by the shielded dose yielded the experimental GPF.

3.4.1 Model Setup and Validation Criterion

The input deck for the initial validation simulation is in Appendix B. In order to keep the model as simple as possible, the corner overlaps were not included. The only physical volumes were the air outside the enclosure, the steel walls of the enclosure (modeled as a single, solid piece with no corner or edge overlaps) and a NaI cylinder suspended in the center of the enclosure. The source was modeled as a point source.

Modeled dose was computed with the F8 tally, which counted photon tracks which deposit energy within the detector volume. A series of energy bins in 10 keV increments allowed the program to produce a spectrum, and multiplying these bins by their medium energy and summing up the resulting product provided a modeled dose. As discussed in Section 1.3, the validation criterion was arbitrarily set as computing the modeled GPF to be within 5% of the measured GPF with 95% confidence or greater. The confidence was computed using the statistical data provided in the MCNP6 output file.

As a check to ensure that the model was simulating actual behavior properly, the experimental and simulated spectra were reproduced using the simulation and experimental results. This allowed side-by-side comparisons to confirm or reject the model's results. These results are discussed in Chapter 5 and the full range of spectra are presented in Appendix A.

3.5 Evaluating Influences on Modeled and Experimental GPFs

The final objective of this work involved several series of simulations and experimental observations. The driving purpose was to investigate the limits of the validation that could be achieved and the effects of different factors upon modeled and

experimental GPFs. The first series studied the effects of different photon energies upon GPFs and the range of photons that upheld the validation criterion. The second examined how different types and levels of model fidelity affected the output of MCNP6. Finally, several series of simulations and experimental observations investigated MCNP6's ability to handle thicker shielding, higher GPFs, and more complicated geometries.

3.5.1 Evaluating GPFs with Different Sources

The first series of the evaluation objective examined the question, "How does validation hold up with other photon energies?" This series retained the same model and experimental settings as the initial validation, with one important difference. In place of the ^{137}Cs source, three alternate sources irradiated the detector in its shielded and un-shielded configurations.

The first alternate source was ^{60}Co, which emits two peaks at the same activity. The first peak is 1173 keV, and the second is at 1332 keV. Both of these peaks are substantially higher in energy than ^{137}Cs's peak of 662 keV. The other two sources were ^{57}Co, which emits photons at 122 and 138 keV, and ^{109}Cd, which emits photons at 88 keV. These peaks, along with their Compton edges, provided insight into how low and high this experimental setup could confirm validation.

3.5.2 Evaluating Model Resolution

The next series in the evaluation objective was conducted with simulations only, and it was intended to investigate the limits of MCNP6 and determine where it breaks down. These limits were evaluated by varying three parameters of the input deck:

geometric fidelity, material data fidelity, and the number of tracks evaluated. Each parameter featured three adjustments to a specific part of the MCNP6 input deck.

Geometric fidelity is a subjective assessment of how closely the cells and their bounding surfaces match the physical reality they are meant to represent in the model. This parameter had three levels of fidelity. The high fidelity model was the initial validation model. The medium fidelity model eliminated the air outside the enclosure and removed the enclosure's wall opposite to the source. The low-fidelity wall removed all walls except the one immediately between the source and the detector, and removed all air, redefining the rest of the problem as a vacuum.

Material data fidelity was a subjective assessment of how closely the model materials matched their chemical and isotopic proportions. The high fidelity model included all elements in a given material making up more than 1% of that material, as well as all isotopes in that element making up more than 1% of that isotope. The medium fidelity model simplified this to the most common isotope of each element. The low fidelity model simplified this still further, so that each material was represented by the most-common isotope of its most common element, except for NaI, which is an even compound of sodium and iodine.

The number of tracks varies the number of primary particles created, as well as all of each primary particle's secondary particles. This varied by powers of 10 from 10^5 to 10^8. The 95% confidence interval of each simulation was calculated from the relative error. By identifying the lowest number of track counts that could meet validation standards, a minimum threshold could be established. This helped the overall work by eliminating unnecessary processing time.

3.5.1 Evaluating the Full-Thickness Assembly

The final series of the evaluation objective challenged MCNP6 to model thicker shielding and more-complicated geometries. It also explored how these geometries affected GPFs. The enclosure was reassembled using all 18 steel plates. Figure 11 shows how the combined thickness of these plates was 1 ¼ inches, which eliminated the corner overlap of the thinner assembly, producing a cubic shield with defined corners and edges.

Figure 11. Scale model of the fully-assembled box

Since higher-energy photons tend to penetrate steel more often and were already validated for the ¼ inch thickness assembly, the ^{137}Cs and ^{60}Co sources were used for this series of observations. The sources were evaluated separately in three locations. Figure 12 shows the placement scheme for the three source positions. The first was face-centered, at the same distance from the center of the detector as in the original experiment, 14 inches. The second was edge-centered, at the same height as in the original experiment, but placed outside the edge, so that the distances from the detector

center to the source along both horizontal axes of the box were 14 inches. The third was outside the corner, such that the distance from the detector to the source along all three axes of the box was 14 inches.
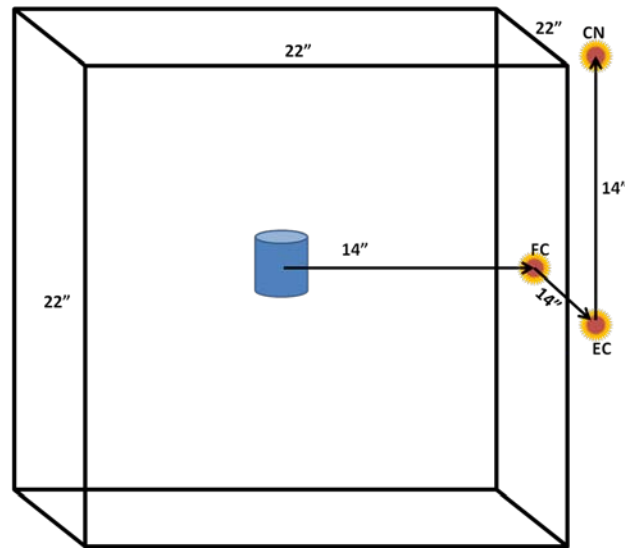
Figure 12. Source placement diagram for the 1 ¼ inch assembly. FC is the face-centered position, EC is the edge-centered position, and CN is the corner position.

The final observation used the two sources simultaneously. The ^{137}Cs was placed at the edge-centered position. The higher energies emitted by the ^{60}Co were expected to penetrate more steel , so the ^{60}Co was placed at the corner. Using the calibrated activities of these two sources, they were modeled in a single MCNP6 simulation.

4. Data Processing

This chapter describes several data processing techniques used in the work. MATLAB served as the post-collection processing platform via several custom-made scripts. These scripts computed dose depositions within the detector, convoluted simulated spectra to provide a convenient comparison between simulation and experimental observations, and produced graphs of these spectra. Additionally, the MCNP6 input decks employed two methods of variance reduction, and Gammavision's settings were adjusted to reduce experimental error by accounting and correcting for dead time.

4.1 Computing Dose

The dose deposited within the simulated NaI detector and the experimental detector were drastically different. MCNP6 normalized all tallies to the total number of primary particles run, whereas the experimental observation is a simple tally for each bin. As a result, the graphs of experimental spectra are labeled as "Number of Interactions" or "Counts per Second," while the graphs of simulated spectra are labeld as "Relative Activity." The gamma protection factor is a unitless ratio that is computed using only simulated spectra or only experimental spectra. Therefore, no conversion is necessary for the tallies.

Computing dose with MCNP6 was a straightforward process. The F8 tally in the output file provided the energy of each bin and its relative activity. Multiplying each energy by its activity yielded a dose associated with that bin. These bin-specific doses

were then summed up to yield a net dose deposited within the simulated detector. This process is represented by

$$\text{Dose} = \sum_{i=1}^{n}(\text{Energy}_i)(\text{Activity}_i), \qquad (17)$$

where n is the total number of bins in the F8 tally. Dividing the dose for a free field simulation by the dose of the associated shielded simulation yields the simulated GPF.

The experimental spectrum posed a complication, as each observation included background radiation. To correct for this, three multi-day observations were taken with no sources present with the detector outside the enclosure, inside the ¼ inch assembly, and inside the 1 ¼ inch assembly. The output file from Gammavision included the observation time with the full array of the tallies recorded in each energy bin. This allowed these background spectra to be normalized by dividing the tally array by the observation time

$$\text{Normalized Background} = \frac{\text{Background}}{\text{Observation Time}}. \qquad (18)$$

The experimental spectra were then corrected using these normalized background spectra. First, the experimental spectra were normalized according to their observation times using the same process as the background spectra. Subtracting the appropriate normalized background spectrum from the normalized experimental observation yielded a corrected, normalized experimental activity.

Using the same equation as the MCNP6 dose calculation, a MATLAB script produced a dose per unit time. The same process was used (with different backgrounds) for shielded and free field observations. The unit of time introduced by the background

39

correction was therefore irrelevant to the overall GPF, as these units divided out to yield a unitless ratio.

4.2 Spectral Analysis and Processing

The validation criterion of this work was a comparison of simulated GPFs and their confidence intervals to a corresponding experimental GPF. This criterion was incomplete, however, without assurances that MCNP6 was modeling the interactions and spectral features identified by the NaI detector system. Such an assurance required the application of signal processing techniques.

When a photon deposits energy into the actual NaI detector, it takes a sequence of subsequent physical interactions to tally that deposition in Gammavision. Many of these processes are inherently imprecise, such as the process in which the photoelectrons created in the detector are multiplied through a series of electric fields. The tendency of the detection system to spread out a signal is described as its response or response function. The NaI detector's response to a discrete peak is a Gaussian distribution about that peak, while MCNP6 will show the discrete peak with no Gaussian distribution. Figure 13 compares an MCNP6 spectrum to an experimental spectrum for similar configurations of sources and detectors.
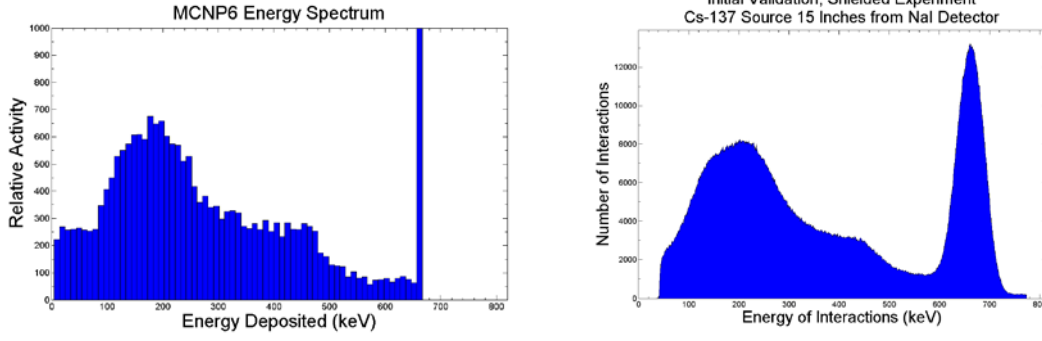
Figure 13. An unprocessed MCNP6 spectrum and an unprocessed experimental spectrum. The maximum peak of the MCNP6 spectrum is well off the scale.

Manipulating the simulation to emulate the response of the detector requires convolution, which is described in Section 2.6. Since ^{137}Cs provides a single 662 keV peak, its maximum peak serves as a convenient source for evaluating the detector response. The full width at half maximum was measured. This value was calculated in terms of the total number of counts detected within the peak as

$$\text{FWHM} = 0.15 * \text{N}, \tag{19}$$

where N is the total number of counts within the peak. Since this peak follows the pattern of a Gaussian distribution, it follows that the standard deviation can be computed as [22]

$$\sigma = \frac{\text{FWHM}}{2\sqrt{2\ln(2)}}, \tag{20}$$

where FWHM is the full width at half maximum and σ is the standard deviation. To apply this to a discrete digital signal, the axis of the signal must be defined as a linear space vector of N points between $-N/2+1$ and $N/2$. This vector is defined in MATLAB as X using the linspace function:

$$\text{X} = \text{linspace(-N/2+1,N/2,N)}. \tag{21}$$

41

The point spread function (PSF) of a Gaussian distribution is then defined as [22]

$$PSF = \frac{1}{\sqrt{2\pi\sigma^2}} e^{-\frac{X^2}{2\sigma^2}}. \tag{22}$$

By taking the Fourier transform of this point spread function, the Fourier transform of the signal, multiplying them together, and taking the inverse Fourier transform of the result, MATLAB generated a padded array containing a convoluted spectrum with the PSF applied to every bin. Once this array was trimmed of the extra 0 value elements and calibrated to the known peak, it produced a simulated spectrum that closely matched the experimental observation, as shown in Figure 14.
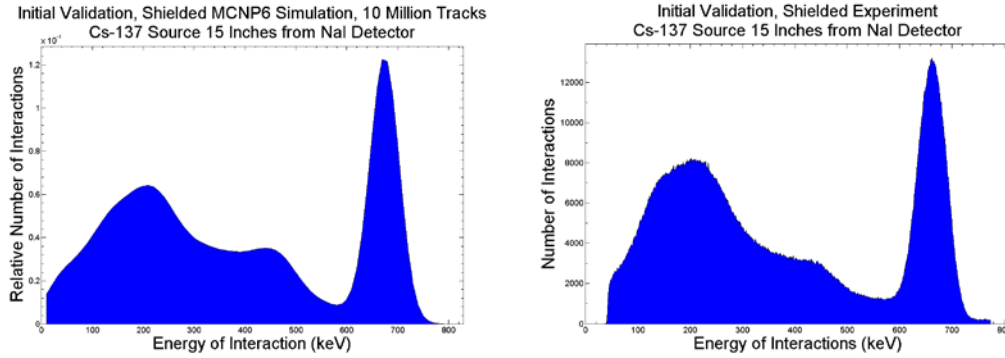
Figure 14. Comparison of a convoluted simulated spectrum (left) with its experimental counterpart (right).

4.3 Variance Reduction

Although it is not a major component of this work's investigation, variance reduction is an important aspect of MCNP6 modeling, and several of its key principles were applied to the simulations. Variance reduction is a collection of processes by which the statistical resolution of data collected can be improved while reducing the overall

computation time of the simulation. There are three principle methods of variance reduction in MCNP6.

The first technique of variance reduction is known as truncation. Truncation is the practice of killing particles that leave the geometry of interest. In this work, the principle of truncation was applied by reducing the surface bounding the problem to be a meter away from the enclosure's inner edge for the ¼ inch assembly, and two meters away from the enclosure's inner edge for the 1 ¼ inch assembly.

Russian roulette and particle splitting involve reducing the computation time associated with regions of low statistical significance. When a particle enters such a region, a weighted random sampling decides whether or not to kill the particle or continue to track it. This is known as Russian roulette. If the tracked particle passes back into a region of interest, it is split into several particles, each of which are then tracked. This is known as particle splitting. In MCNP6, these practices are done by adjusting the importance of a cell. For example, in the 1 ¼ inch assembly model, a concrete room was modeled around the enclosure. This increased the simulation run time on the laptop computer used from 88 seconds to 547 seconds. By assigning an importance of .1 to the concrete cell, and an importance of 1 to everything else, the runtime was reduced to 152 seconds, while the statistical variance in the detection cell was unchanged.

4.4 Eliminating Dead Time

As discussed in Chapter 2, the dead time of a detector is an important feature in the validation that is not modeled in MCNP6. This is a particularly concerning factor for experiments in which detectors experience very high dose rates. If not considered and

corrected for, this could be a problem for unshielded detectors. Fortunately, most spectral software keeps track of the dead time, allowing the flux to be corrected with a simple operation for each energy bin:

$$\text{Counts}_{\text{Corrected}} = \text{Counts}_{\text{Raw}} * \frac{\text{Time}_{\text{Observed}}}{\text{Time}_{\text{Observed}} - \text{Time}_{\text{Dead}}}. \tag{23}$$

Gammavision was set to apply this correction to all experimental spectra taken.

5. *Results and Analysis*

This chapter presents results of models, experiments, and data processing to support the three objectives of this work: verifying MCNP6 as a good choice for GPF computation against other approaches and models, validating MCNP6 for GPF computation with a simple experiment, and evaluating the influences of different factors upon validation and GPFs. Results supporting the objective of verifying MCNP6 as a valid modeling choice are presented in Sections 5.1 and 5.2. Section 5.3 validates MCNP6 against a simple experiment. Sections 5.4 through 5.8 evaluate the influences of several factors upon validation and GPFs.

5.1 Comparison of Analytical and Quadrature Models to MCNP6

The Mathematica model was set to have an initial flux of 100 keV photons through a 1 cm iron barrier. The analytical portion of this model provided a means for direct quantitative comparison with MCNP6. For the Mathematica model, a "Peak GPF" was computed by dividing the attenuated flux by the original flux.

In MCNP6, a 1 cm-thick slab was placed between a source and a NaI cylinder. Two simulations were run, one with the barrier and one without. Both simulations tallied the full-peak photon energy depositions inside the simulated detector. The unshielded peak activity was then divided by the shielded peak activity. The results of the MCNP6 simulation and the analytical simulation are in Table 1. The 95% confidence interval for the MCNP6 result is two standard deviations, while the analytical result is not derived from statistics and therefore has no confidence interval.

Table 1. Peak gamma protection factors for MCNP6 and the analytical model.

	Peak GPF	2σ
Analytical	1.783	N/A
MCNP6	1.746	0.0028
%Difference	2.12	

This comparison verified MCNP6's peak attenuation. However, it provided no information on the scattered photons. The scattered photons were modeled in Mathematica through two successive Compton scatterings.

All of the photons that attenuated through the barrier were assumed to Compton scatter. The first scattering was modeled as happening in the center of the barrier, and the second was modeled as happening ¾ of the way through the barrier. Figure 15 shows the binned photons escaping after the first two scatterings. The second-scatter escapes are more plentiful than the first due to the fact that they had only half the thickness of iron left to penetrate.
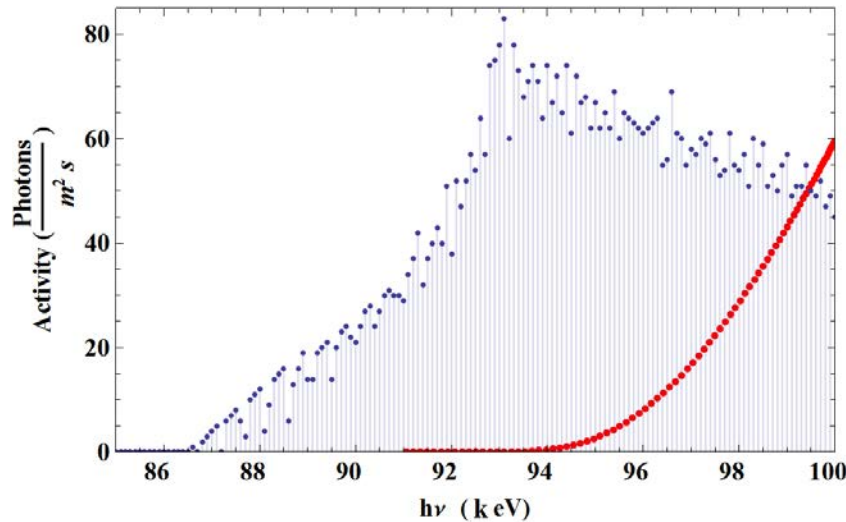
Figure 15. Binned photon energy groups that pass through the iron barrier after one scattering event (red) and two scattering events (blue).

The spectrum produced by the first two scatterings shows some interesting differences between the first and second scatterings. In particular, the second scattering activity peaks at a lower energy, while the first scattering peak is essentially at the original peak energy. This demonstrates the beginnings of what would likely develop into an escape peak from the iron. Further scatterings, however, proved to be impractical to model.

The first scattering required Mathematica to calculate the probability of 180 degrees of scattering angles in 180 separate groups. These groups were then attenuated through the remaining half of the barrier. For the second scattering, the attenuated portions of these 180 groups had to be divided again with 180 subgroups for each of the original 180 groups. Additionally, the scattering angle had to be revolved around the axis of the incident photon in accordance with the Law of Cosines for Spherical Triangles described in Chapter 2. This required each subgroup to be divided into 360 sub-subgroups. Each sub-subgroup then had to be attenuated through the remaining quarter of the barrier. Any further scatterings would have required 64,800 times as many calculations as the one before it.

This geometric rise in required computing became impractical beyond two successive scatterings. Using an Intel Core i5-2520M CPU at 2.5GHz with 4 GB of RAM and no other active programs, Mathematica took 150 minutes to generate the outcome of two successive scatterings. Another scattering would increase this time to 18.5 years. Although this program could be improved by eliminating groups with activities below a certain threshold and using fewer groups per scattering, the geometric expansion of

computing time for successive Compton scatters would remain. Without more Compton scatters, the program could not produce a comparable spectrum to MCNP6. Without similar spectral behavior between the two models, there was no basis to perform a meaningful quantitative GPF comparison. These results were useful for understanding some of the phenomena of photon interactions, but they were not useful for modeling GPFs.

Furthermore, the model was inflexible and required extensive retooling to change between different materials. It could not model complex geometries, and its file size was 1.1 megabytes, as compared to an MCNP input file of 15 kilobytes. Finally, Mathematica itself is expensive, costing $2,250 for a standard government license [12]. By contrast, MCNP6 is available upon request from LANL and does not require additional taxpayer funding.

5.2 Comparison of Other Monte Carlo Models to MCNP6

Since the MATLAB slab-geometry Monte Carlo program was not limited to a certain number of successive interactions, it produced a spectrum that was more comparable to the MCNP6 model than the Mathematica approach. The spectrum produced was a binned tally of the energies of photons crossing a 2-dimensional barrier between two iron barriers. Figure 16 compares the MATLAB Monte Carlo simulation's spectrum to an MCNP6 tally of photons crossing the surface of a detector within an analogous steel enclosure.
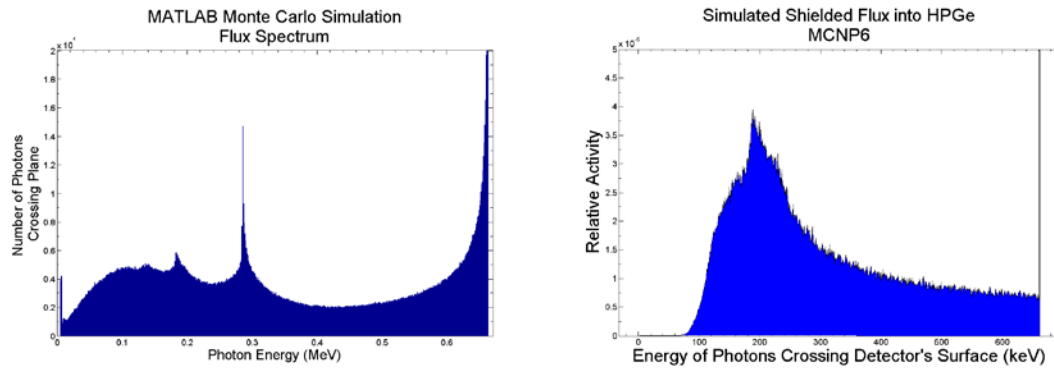
Figure 16. MATLAB Monte Carlo script output, simulating the photon flux between two iron barriers (left) and MCNP6 simulation of photon flux into a detector (right).

Although both spectra show an escape peak just under 200 keV, the MATLAB model also shows a larger peak at 300 keV and a high-energy activity that rises gradually to the peak. Neither of these behaviors is supported by theory. The cause of this behavior was not determined, but it was likely due to a bug in the transport code or a side-effect of using slab geometry. Without similar spectral behavior between the two models, there was no basis to perform a meaningful quantitative GPF comparison.

Qualitatively, MATLAB offered some significant benefits, including easy debugging features, excellent native graphing tools, and a code structure that was short and easy to examine in detail. Further work might well be able to improve the model. However, even with its current issues resolved, the slab geometry model could not account for complex 3-dimensional shapes or model any other interactions besides Compton scattering. The model would also require significant reprogramming for different layer configurations, materials, and tallies. The MATLAB model was also less efficient than MCNP6 for large track numbers. While using the same processor with no other programs running, a simulation of 10 million tracks took MCNP6 two minutes,

while the MATLAB code required two hours. Finally, MATLAB costs $2,150 per government or commercial license, while MCNP6 is free [21].

Of the modeling options examined, GEANT4 comes closest to MCNP6 in overall performance. Both are available at no cost, and both can model a wide variety of particles through three dimensional geometries and complex materials. In some ways, GEANT4 is superior to MCNP6. For example, it retains individual particle track information, and its native visualization allows users to ensure a correct geometric configuration and view particle tracks directly, as seen in Figure 17.
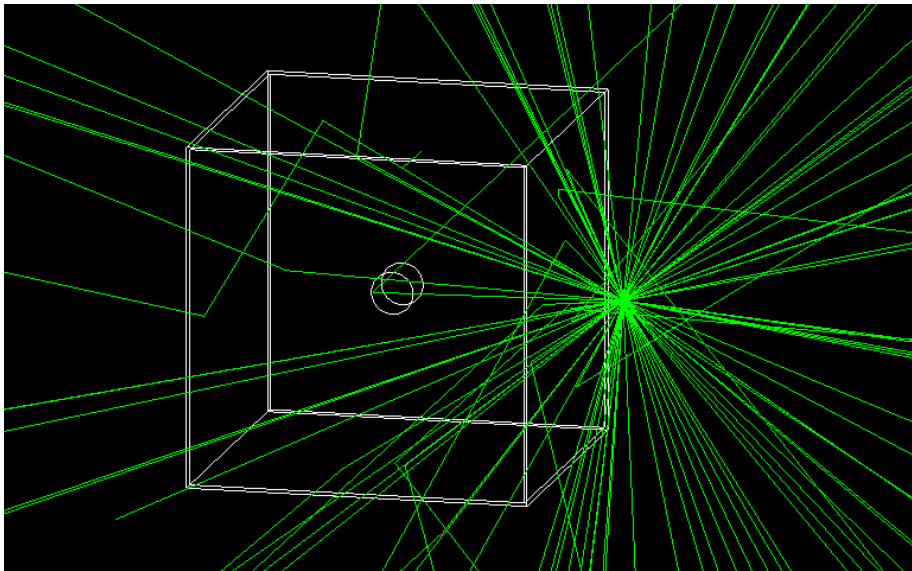
Figure 17. GEANT4 visualization of the model with some demonstration photon tracks. The source is outside the box, on a center line with the nearest face. Inside is a NaI cylinder.

The identical inputs to GEANT4 and MCNP6 yielded energy deposition spectra in the NaI detector volumes. Both spectra were plotted in 67 energy bins 10 keV wide as shown in Figure 18.
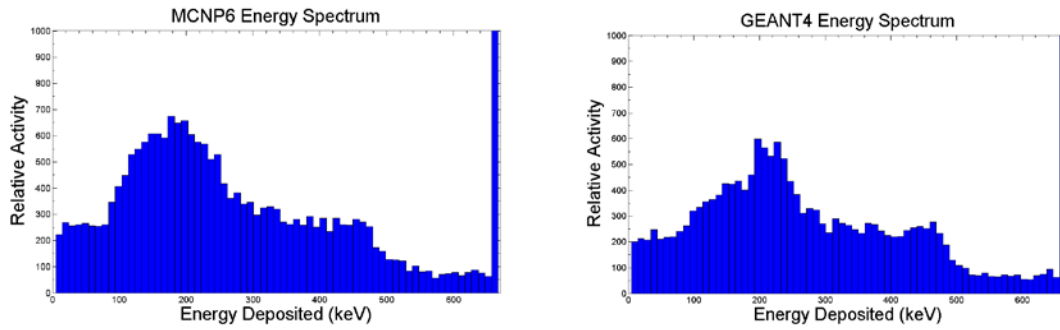
Figure 18. Photon energy deposition spectra for identical inputs to MCNP6 (left) and GEANT4 (right). The peak spectra at 662 keV are cut off in order to show down-scattered photon energy spectra.

A cursory examination of these spectra highlights their similar features. Both models produced peaks at 662 keV, Compton edges at 460 keV, and build up regions at the same photon energies around 200 keV. The overall shapes of the spectra match up well. Figure 19 plots the difference in each bin from GEANT5 to MCNP6. Only one bin differs by more than 50% from its counterpart in the other spectrum.
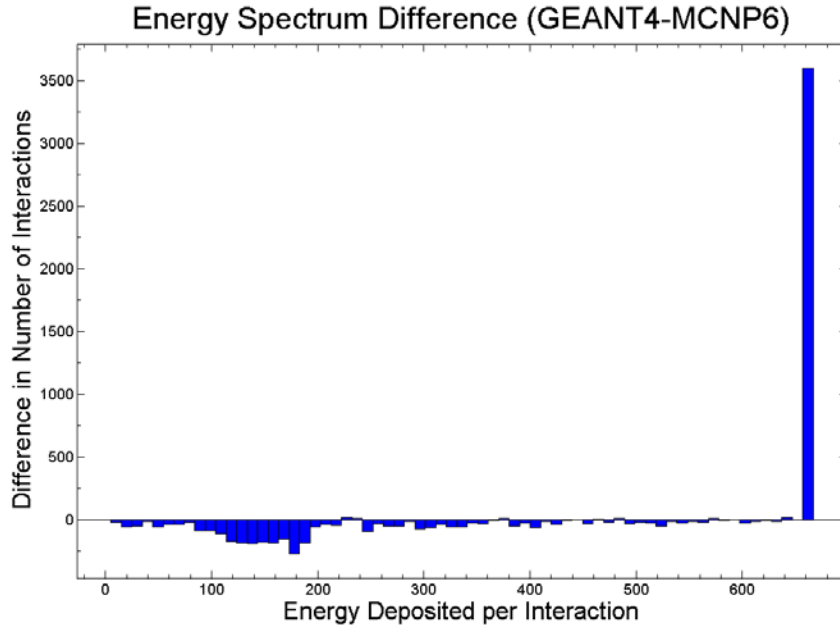
Figure 19. A difference plot between the GEANT4 energy deposition spectrum and the MCNP6 energy deposition spectrum. Ideally, this would be a flat line at zero.

The primary discrepancy between these spectra was the peak monoenergetic photons that passed through the iron without interacting and deposited all their energy inside the detector volume. GEANT4 showed 9,186 interactions, while MCNP6 showed only 5,589. Additionally, there is a sudden drop off in the GEANT4 spectrum's lower-energy build-up region that is not present in the same region of the MCNP6 region.

One possible discrepancy between the two codes is that GEANT4 is configured to track electrons, while MCNP6, for this run, was not. However, this explains neither the difference in peak photon counts nor the different build-up region shapes, since tracking secondary electrons would result in GEANT4 having more activity at lower energy levels, and not less. Another possible explanation is an error in one of the simulation files for GEANT4, which requires significantly more programming than MCNP6.

It is difficult to assess which model is more correct by inspection of the spectra, since no detector will give a perfect, 100% efficient energy collection with perfect resolution. However, it is possible to predict the actual detector spectrum using signal processing techniques. Using the detector's measured full width half maximum of a known photopeak for a radioactive isotope, it is possible to construct a system response as a point spread function for the detection system. Convoluting the simulated spectrum with this point spread function yields a close approximation of a NaI detector spectrum.
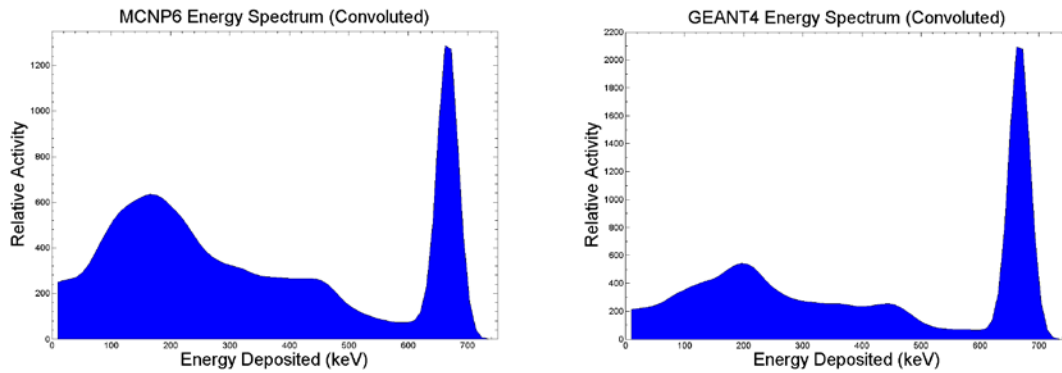
Figure 20. A comparison of energy deposition spectra convoluted with a point spread function to simulate an actual NaI detector.

Figure 20 shows the two simulators' convoluted spectra. Comparing later experimental spectra to these convoluted simulation spectra indicated that the MCNP6 simulation was a better representation of reality. However, for the purposes of this work, either model might produce valid GPFs regardless of the outcome of such a comparison, as long as the modeled ratio of shielded dose to unshielded dose is consistent with experimental results.

5.3 Initial Validation Experiment: NaI

Comparing dose depositions with MCNP6 to the dose detected in experimentally shielded and unshielded configurations yielded GPFs with a difference of 3.4% for the NaI detector. The high number of MCNP6 tracks and large number of interactions measured reduced the variance to negligible levels; this is explained in detail in Section 5.5.3. Therefore, MCNP6 met the validation criteria for this experiment established in Section 2.7.

Table 1 presents the experimental and modeled GPFs, as well as their 95% confidence intervals, defined as the region within two standard deviations of the GPF presented. Since GPFs are dose ratios, no units are necessary for this comparison.

Table 2. Initial validation results

	MCNP6	Experimental
GPF	1.0225	1.0587
$\pm 2\,\sigma$	0.0016	0.0053

In this case, a simple ratio comparison raises some logical concerns about the reliability of this evaluation. After all, dividing the dose deposited from one free-field measurement by an identical measurement would yield a GPF of 1, which is almost within the validation criterion. Therefore, while the GPF comparison met the validation threshold, it requires some supporting spectral comparisons.

Figure 21 and Figure 22 show a direct comparison between spectra created from MCNP6 data and spectra taken experimentally. The consistency of their peaks and

Compton edges supports the GPF validation. However, there are some interesting, if minor, discrepancies.
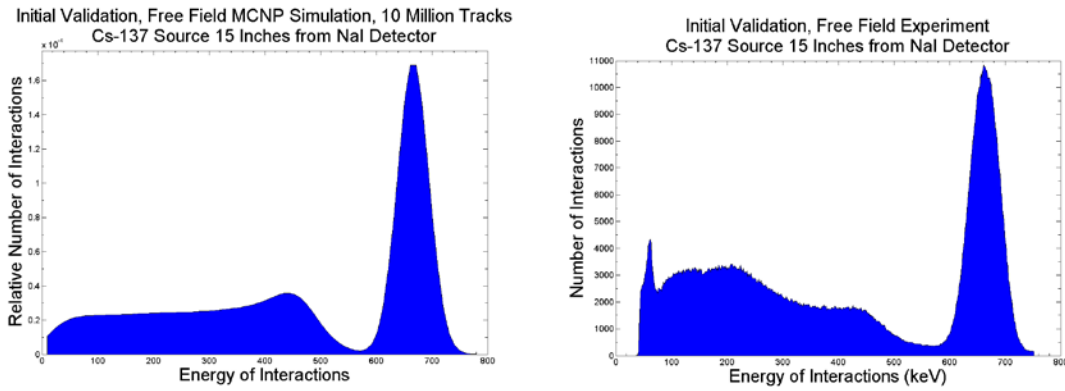
Figure 21. Simulated (left) and experimental (right) spectra for a free-field configuration. The simulated spectrum has been convoluted with a point-spread function to generate an ideal NaI response. The experimental results do not include the lowest energy bins, as these tend to become saturated with electronic noise.

Although these results met expectations, several differences bear mentioning. The free-field spectra of the MCNP6 and experimental results show identical energy values for the peak and Compton edge, but the experimental results show some build-up at lower energies, as well as a very low-energy peak. A combination of background radiation and photon interactions with the nearby concrete and low-energy phosphorescence in the detector are the likely causes of these discrepancies. Since these discrepancies occur in the low-energy bins, they have little impact on the overall dose or GPF.

These discrepancies were notably absent in the experimental shielded spectrum, which closely matched the simulated spectrum's features as shown in Figure 22. The only notable difference was a lower-energy build-up region with noticeably more interactions for the experimental results than the simulated results. Since this discrepancy paralleled

the increased low-energy interactions of the free field experimental spectrum, the overall

GPF remained consistent.
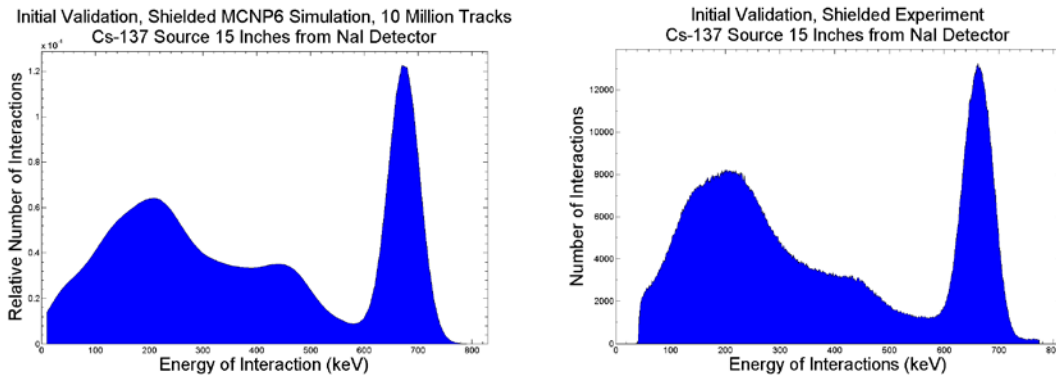
Figure 22. Simulated (left) and experimental (right) spectra for a shielded configuration. The simulated spectrum has been convoluted with a point-spread function to generate an ideal NaI response. The experimental results do not include the lowest energy bins, as these tend to become saturated with electronic noise.

The limitations of the equipment itself create additional sources of error. The response function of the detector spread the 662 keV single energy peak more than the experimentally-derived point spread function used to convolute the model results. This is likely due to fluctuations in the power supply. Additionally, the lowest energy bins had to be truncated, as these bins tended to become saturated with electronic noise and phosphorescence from the NaI. Additionally, these spectra were calibrated only with the 662 keV energy peak with the assumption that the NaI detector had a linear response function. A more thorough multi-peak calibration could match the energy bins somewhat more precisely. Although both of these could have been corrected with additional equipment and a more extensive series of calibration runs, neither factor prevented validation, so their role was considered negligible for the purposes of this study.

5.4 Initial Validation Experiment: HPGe

The energy-dependent efficiency of the germanium detector prevented an experimental validation of MCNP6. The semiconductor properties, and not the material absorption cross-sections, drive the energy-dependence of the germanium detector. Therefore, the dose deposition provided by MCNP6 did not match the output of the germanium detector. The experimentally-derived GPF was 1.202, and the output spectra are shown in Figure 23.
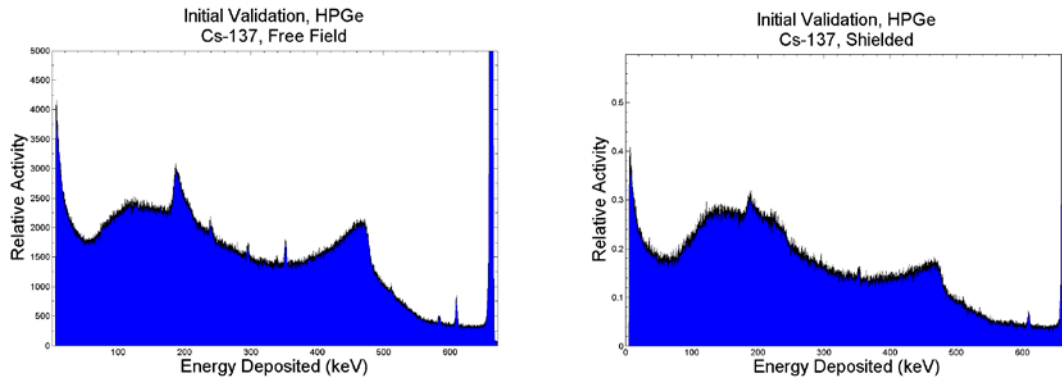
Figure 23. Experimental spectra from a HPGe detector using an identical source in an unshielded (left) and shielded (right) configuration.
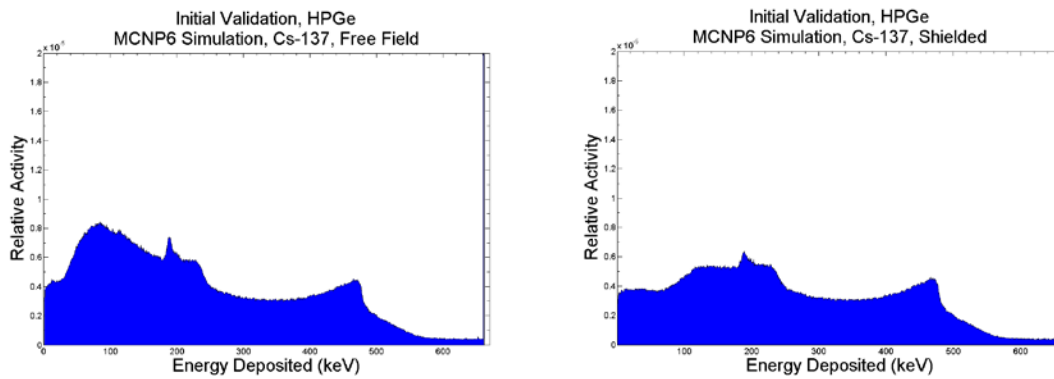
Figure 24. MCNP6 of the HPGe detector in the free field (left) and shielded (right) spectra using the dose-deposition tally. Note the clear Compton edge and continuum.

A multinuclide source allowed for an energy-based efficiency calibration; this calibration compared a flux of known photon peak activities to detected peak activities. This process inherently included the influence of material photon absorption cross sections. Figure 24 shows the MCNP6 simulations' dose-deposition spectra. Although the 662 keV peak, Compton edge, and escape peak from the air and iron were at the correct energies, the shapes of the models differed. The proportions of the modeled features in Figure 24 did not match up to the proportions of their experimental counterparts in Figure 23. This resulted in a GPF of 1.042, nearly 15% less than the experimental results.

A logical next step was to simply tally the photon flux into the model detector and apply an experimentally-derived efficiency calibration. This solution did not yield usable results either. Although the photon peak was adjusted appropriately to account for the efficiency calibration, the calibration did not account for spectroscopic features associated with Compton scattering inside the detector. Without a Compton edge or continuum, the result did not include the physics necessary to compute a valid dose or GPF. Figure 25 shows the modeled flux spectrum with the energy calibration applied. Although this does show the escape peak from Compton interactions in the iron and air, the lack of lower-energy Compton features from interactions inside the detector reduced the resulting GPF to 0.977 for this approach, 23% lower than the experimental results.
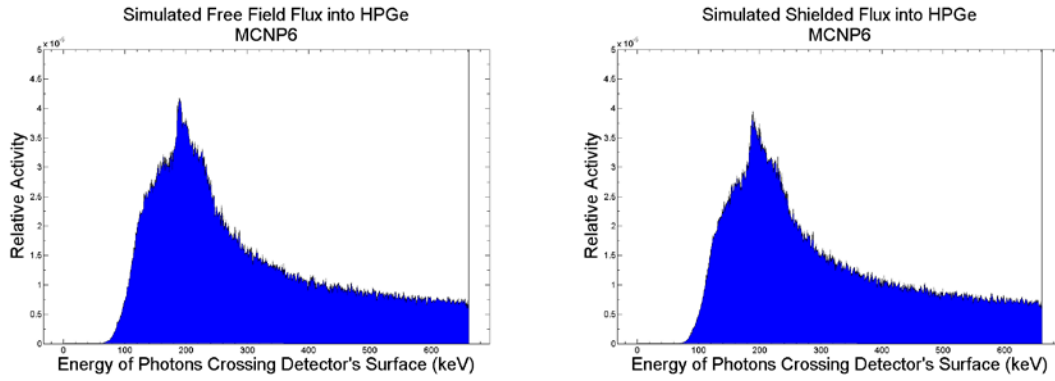
Figure 25. Simulated photon flux spectra from the free field (left) and shielded (right) configurations, adjusted with an experimentally-derived efficiency calibration. Note the lack of Compton edges or continua.

The fundamental issue with validating MCNP6 with a germanium detector comes from the nature of the semiconductor detector itself. Although the high resolution of this detector allows for precise peak identification, its efficiency is a function of several factors, including the photon attenuation properties of germanium, the electronic properties of the germanium for moving charges, the locations and sizes of the p and n-type regions within the detector, the geometry of the detector, the temperature of the Sterling engine-cooled detector, and the stability of the bias power supply.

Figure 26 shows an experimentally-derived energy-dependent efficiency of the germanium detector. This efficiency curve includes the relevant factors and can be applied to a known source or flux to predict the output of the detector. However, it yielded invalid results when applied to the simulated spectra.

59
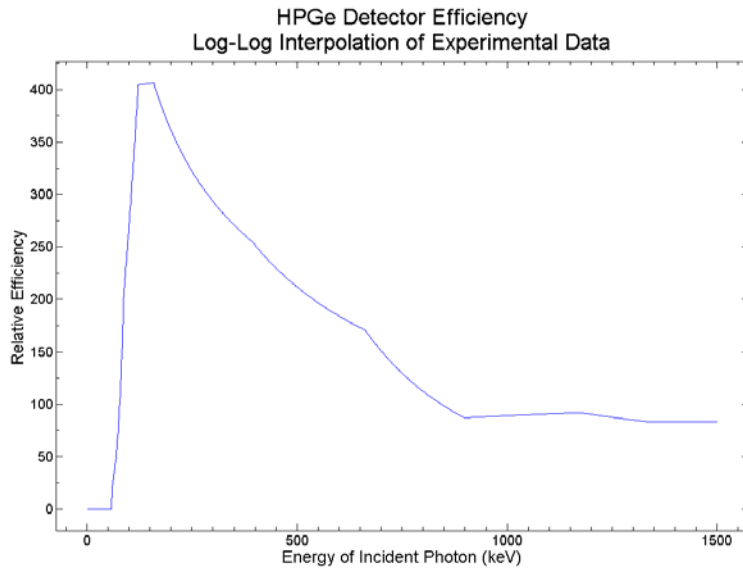
Figure 26. Experimental efficiency calibration for the germanium detector.

In order to validate MCNP6 for dose depositions inside a germanium detector, the geometric and X-ray attenuation properties would have to be segregated into a discrete efficiency function from the electronic efficiency of the detector. This would require the development of a signal processing algorithm, and that algorithm would also have to be verified and validated experimentally. While such a study could be a useful topic for future research, it was beyond the scope of this project. Since the NaI detector offered a more straightforward approach for validation, it was the only detector used in the remainder of the observations taken.

5.5 Modeling Resolution

5.5.1   Geometry Resolution

Since the initial validation was successful, a series of alterations reduced the geometric fidelity of the model to the experiment to find a "breaking point." These alterations were grouped together into two categories. Each category was evaluated at three levels of fidelity.

The first category of model resolution was geometrical. Since the initial validation was valid, its input deck was adopted as the "high fidelity" run. The "medium fidelity" run removed the far-side plate of the box and eliminated all air outside the box. The "low fidelity" eliminated all but the single panel of the box between the source and the NaI detector and replaced all air with vacuum.

Table 3. GPFs produced in MCNP6 with varying degrees of geometric fidelity to the problem.

Fidelity	GPF	$\pm 2\,\sigma$
High	1.021	0.022
Medium	1.031	0.022
Low	1.098	0.024

The GPFs in Table 1 produced by the medium and low resolution models differed from that produced by the high fidelity model. However, when compared to the experimental GPF of 1.0587 from the initial validation experiment, all three models met the validation criteria. While MCNP6 produced virtually identical dose deposition spectra for all three fidelity levels in the free field configurations, the shielded spectra of Figure 27 differ significantly in the low fidelity case. This suggests that a reliable GPF may be obtainable from geometric approximations of an actual vehicle, but a simple barrier would not sufficiently model GPFs of a three-dimensional body, such as an armored vehicle.
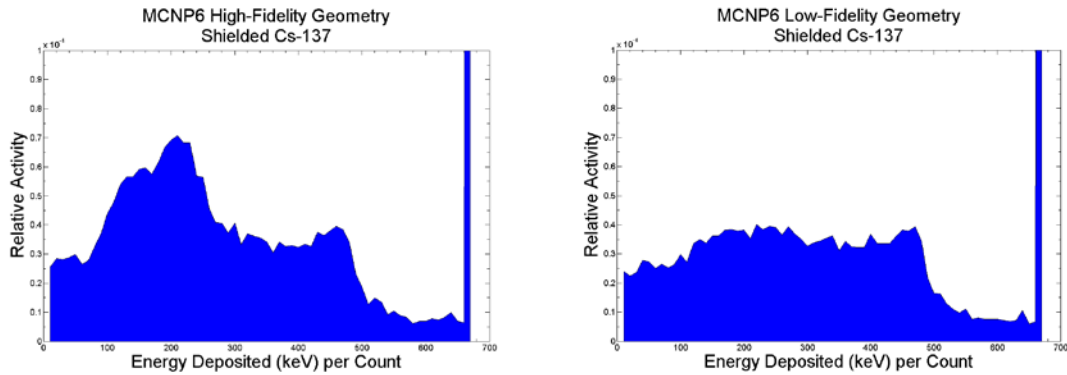
Figure 27. Comparison of MCNP6 spectra with geometries in the high-fidelity (left) and low fidelity (right) settings. The windows of both are cutting off the full height of the full-energy peaks in order to highlight the differences in the lower energy ranges.

5.5.2   *Material Data Resolution*

The second category of model resolution studied focused on the material data cards. The "high fidelity" evaluation included each element's natural isotopes in their normal relative abundance. The "medium fidelity" evaluation simplified each element to its most-common isotope. The "low fidelity" evaluation eliminated all but the most common material in each cell with the exception of the NaI, which contains an even mix of sodium and iodine atoms.

Table 4. GPFs produced in MCNP6 with varying degrees of material fidelity to the problem.

Fidelity	GPF	±2σ
High	1.021	0.016
Medium	1.021	0.015
Low	1.023	0.017

Varying the material data fidelity had little effect on the GPF. The spectra produced were virtually identical. The only noticeable spectral difference was a sharpening of low-energy escape peaks in the shielded configuration as the iron was simplified to a monoisotopic approximation. While Figure 28 illustrates this difference, it also shows little change to the overall shape of the spectrum. It follows that simplifying the materials has little effect upon the overall dose or GPF.
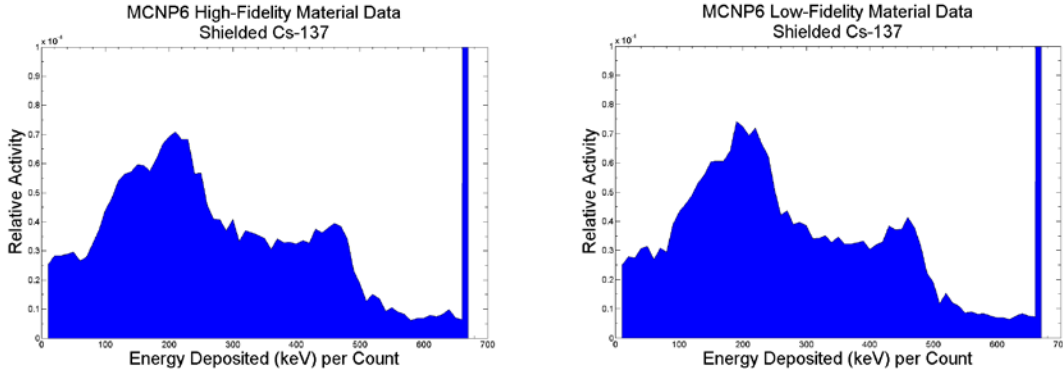
Figure 28. MCNP Shielded Spectra with high material fidelity (left) and low material fidelity (right). The shape of the escape peaks around 200keV is the only significant difference.

5.5.3   Statistical Resolution

The final category of model resolution studied the influence of the track count on the model's GPF. The "high fidelity" evaluation had 100 million tracks and tallied energy

depositions per track in 1 keV bins. The "medium fidelity" evaluation had 10 million tracks and tallied energy depositions per track in 10 keV bins. The "low fidelity" evaluation had 100,000 tracks and tallied energy depositions per track in 100 keV bins.

The track numbers of the simulations, the run times of the experiments, and the bin widths of both drove the statistical variance of the MCNP6 models and experimental spectra. MCNP6 output files' dose deposition tallies provided the energy, activity, and relative error of each bin in its output file. The relative error is defined as [22]

$$\mathrm{Re}lativeError = \frac{\sigma_{\bar{x}}}{\bar{x}}$$

where $\sigma_{\bar{x}}$ is the standard deviation for that bin's tally and $\bar{x}$ is the mean activity for that bin. The relative error describes the precision of an individual energy bin, and not the overall dose, and the overall dose is the value of interest to this work. An effective method for evaluating the overall error for a GPF is to observe the highest peak bins in the free field and shielded simulations of a GPF calculation. Multiplying the higher of these two relative errors by the GPF will yield a worst-case approximation of the GPF's standard deviation.

The data below suggests an inverse square root relationship between the dose's standard deviation and the track count. Since 95% confidence is the threshold for validation for this work, the modeled GPF ± 2 standard deviations should lie entirely within the measured GPF ± 5% according to the 68-95-99.7 rule [6]. The initial validation's 10 million tracks is high enough to meet the validation standard, while a run of 1 million tracks was not, as its confidence interval's lower bound was below 95% of the experimental GPF.

Table 5. Statistical data from the MCNP6 track count study. Track counts meeting the validation criteria must have their confidence intervals bounded between the experimental GPF $\pm$ 5%, or between 1.0058 and 1.1116

Number of Tracks	Free Field % Relative Error	Shielded % Relative Error	GPF	Lower Bound Confidence Interval	Upper Bound Confidence Interval
100000000	0.29	0.0034	1.023	1.016044	1.029956
10000000	1.08	0.009	1.0203	1.001935	1.038665
1000000	0.0267	0.034	1.0053	0.93694	1.07366
100000	0.0924	0.1066	0.9413	0.740615	1.141985

Although the initial validation experiment was successful, and closely matched the shape of the experiment with an appropriate point spread function applied, the spectrum produced by the initial MCNP6 simulation had bins 10 keV wide, which was adequate to match the low-resolution results of the NaI detector. However, MCNP6 can tally in bins far smaller than 10 keV. In an effort to achieve a closer GPF match to experimental results, the input deck was adjusted to output dose depositions in 1 keV increments, while the number of tracks was increased to 100 million. With these settings, MCNP6 produced a GPF of 1.022. Since this result matches what was obtained using a lower-fidelity approach, this higher-resolution approach was of little use for calculating GPFs. However, this high-resolution technique produced spectral features that confirmed MCNP6's ability to model different mechanisms of photon transport, which are addressed in the next section.

5.6 Confirmation of Characteristic X-rays and Pair Production

An interesting feature appeared when evaluating MCNP6 spectra at this higher resolution and track count. When using a dose deposition tally of 1 keV bin increments for 100 million tracks or more in a cylinder of NaI using a ^{60}Co source, four anomalous, small peaks appear in the resulting spectrum of Figure 29. Two of them can be explained by pair production: an escape peak from the iron box at 511 keV, and an escape peak from the detector at 823 keV, which is 511 keV less than the 1332 peak. However, pair production cannot explain why a small but distinct a "shadow peak" occurred below each known peak. In every case, the shadow peak was over an order of magnitude greater in activity than the bins to its left and right, and it was precisely 28 keV less than the main peak.
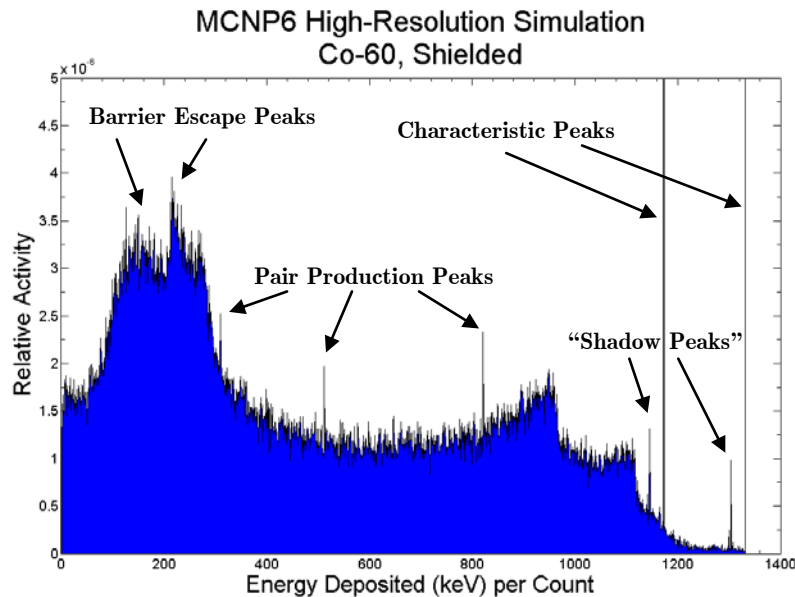
Figure 29. High-resolution MCNP6 spectrum for ^{60}Co in a shielded environment. Note the "shadow peaks" at fixed intervals below both characteristic peaks for the ^{60}Co.

The "shadow peak" is an escape peak caused by a characteristic X-ray escaping the NaI. When a peak photon deposits all its energy inside the NaI detector, it can excite an L-shell electron of the iodine into the K shell. This process emits a 28 keV X-ray [5]. When this photon escapes, it diminishes the resulting peak energy deposited by 28 keV. Although the escape peak's low activity prevents a significant effect on the overall GPF, its presence demonstrates MCNP6's ability to model material-dependent characteristic X-rays.

This higher-resolution approach also allows for a more definitive identification of peaks associated with pair production events. Increasing the energy of the photons to 4 MeV drove pair production to become a dominant effect in the dose deposition spectrum. Figure 30 demonstrates this by convoluting the MCNP6 spectrum with the NaI detector response. Escape peaks at 511 and 1022 keV less than the primary peak, as well as the 511 keV escape peak, demonstrate pair production's dominance as a photon transport mechanism in this scenario.
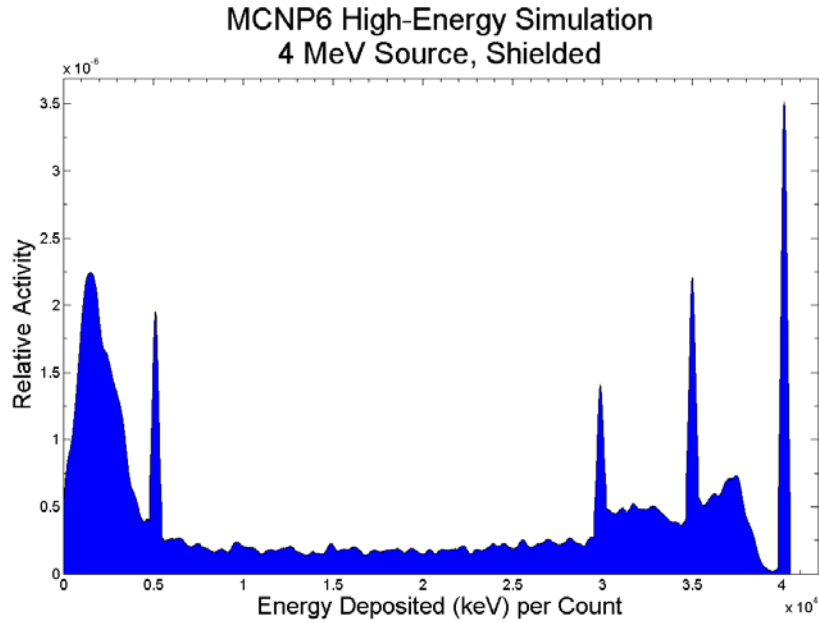
Figure 30. MCNP6 Dose Deposition Spectrum for a modified version of the Initial Validation model. The primary photon energy has been increased to 4.0 MeV, and the bins are 1 keV wide. The MCNP6 output has been convoluted with a point spread function to simulate an expected NaI output.

Practical concerns impeded the experimental validation of these transport mechanisms. The NaI detector's large size prevented most characteristic X-rays from escaping, and its resolution was too low to differentiate between the true peak and the escape peak. Validating pair production was complicated, as the only 4 MeV source readily available at AFIT was a PuBe source, which also produces significant amounts of neutrons and other gamma rays.

Although both of these mechanisms might merit further investigation for validating photon transport, GPF validation required validated aggregate results, not specific mechanisms. Therefore, neither effect merited further investigation in the context of this work.

5.7 Alternate Source Evaluations

Following the initial validation experiment, several sources were substituted for the ^{137}Cs using the NaI detector and the iron box in its ¼ inch wall thickness configuration, and these sources were simulated in MCNP6. For the higher-energy sources, the MCNP6 GPFs met the validation criteria when compared to the experimental GPFs.

Table 6. Alternate source GPF Evaluations.

Source	High Peak	Modeled GPF	Model GPF ±2σ	Experimental GPF	Experimental GPF ±2σ
^{60}Co	1332	1.052	0.0231	1.054	0.0116
^{137}Cs	662 keV	1.022	0.0225	1.068	0.0117
^{57}Co	123 keV	2.457	0.0541	4.065	0.0447
^{109}Cd	88 keV	6.89	0.152	3.45	0.0380

The ^{57}Co and ^{109}Cd source experiments did not validate their respective models. This is due to the vast majority of the scattered photons produced by these sources falling under 80 keV, which was too low for the NaI detector's threshold.

One interesting result from this study was that ^{60}Co GPF approximately matched (and slightly exceeded in the model) the ^{137}Cs GPF, despite its much-higher photon energy and corresponding lower material cross sections. The energy dependence of the Klein-Nishina distribution explains this behavior. At the 1173 and 1332 keV energies emitted by ^{60}Co, Compton scattering will tend to deflect photons at small angles, while the lower energies of ^{137}Cs tends to deflect at wider angles. The lower-energy photons of the ^{137}Cs will tend to scatter off the walls of the walls of the box toward the detector more often than the primary photons coming from the ^{60}Co.

5.8 Thick-Wall Assembly Experiments and Models

The iron box was then reassembled to its maximum wall thickness of 1¼ inches and tested in a variety of configurations to demonstrate MCNP6's ability to model scenarios with complicated geometries and sources. Due to the need for a stronger table for the box and better shielding for the longer observation times required, the box was moved into a smaller, concrete-enclosed room. This caused significantly more lower-energy activity in the "free field" measurements due to scattering off the walls, so the room was modeled as a concrete box around a box of air containing the steel enclosure. Since little of the lower-energy sources' photons penetrated the thin-wall configuration, only ^{137}Cs and ^{60}Co were used for evaluating the thick-wall assembly. Sources were placed either outside the center of a face, outside the center of the edge, or outside a corner, as shown in Figure 31.
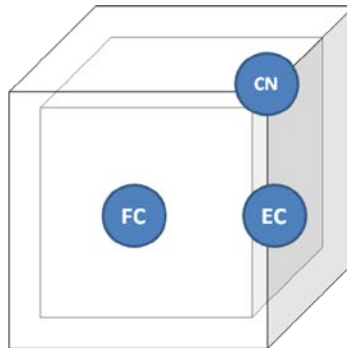
Figure 31. Placement of sources for the thick-assembly observations and models. FC is face-centered, EC is edge-centered, and CN is corner. The source is placed 14 inches from the center of the detector in along one, two, and all three axes of the box, respectively.

Figure 32 and Figure 33 demonstrate how the experimental spectra for the free field and shielded configurations of the thick box experiments closely matched their

MCNP6 simulations. See Appendix A for the other thick-wall assembly experimental and MCNP6 spectra. Similar to the initial validation experiment, the discrepancies were most-noticeable in the lower-energy regions of the free field observations, where the experimental spectra showed more activity than the models. As noted in Section 5.3, this is likely driven by characteristics of the detector system.

The first evaluation was a series of observations similar to the initial validation experiment. This evaluation produced GPFs for a ^{137}Cs and ^{60}Co source just outside the center of the box's face. Table 7 contains the experimental GPFs and their corresponding GPFs produced in MCNP6.
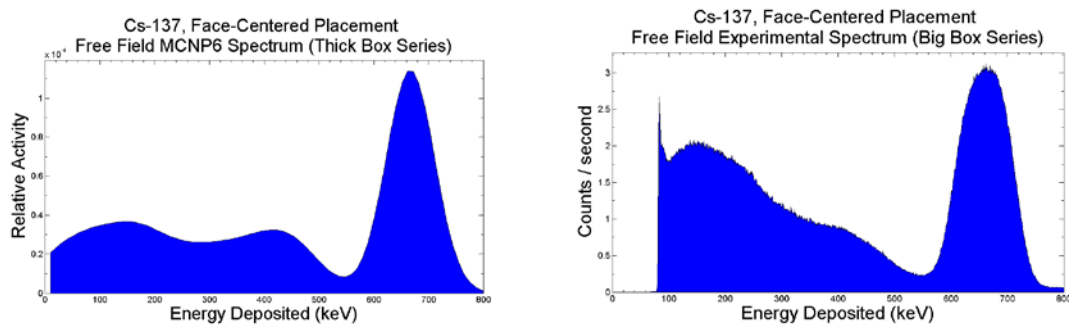
Figure 32. Comparison of free field MCNP6 simulation (left) and the corresponding experimental observation (right), for the thick-box, face-centered ^{137}Cs evaluation.
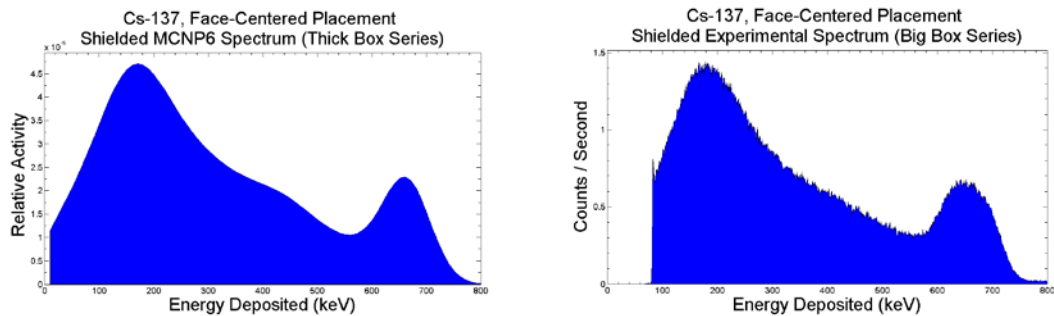
Figure 33. Comparison of shielded MCNP6 simulation (left) and the corresponding experimental observation (right), for the thick-box, face-centered ^{137}Cs evaluation.

Table 7. Experimental and MCNP Gamma Protection Factors for face-centered sources outside the thick-assembly box.

Source	^{60}Co	^{137}Cs
Model GPF	1.76	2.16
Model GPF ±2σ	0.034	0.042
Experimental GPF	1.83	2.12
Experimental ±2σ	0.013	0.018

The thicker walls attenuate the peak-energy photons more and block much of the down-scattered low-energy build-up region. While this lower-energy region remains active in the shielded configurations, the thicker iron results in fewer photons escaping from the iron after undergoing Compton interactions. Thus, the thicker walls result in significantly higher GPFs than in the thin-wall assembly for both the ^{60}Co and the ^{137}Cs as shown in Table 7. By making the walls five times thicker, the GPF for these higher-energy photons has gone from a nearly worthless protection factor very close to 1 to a better, if still modest value.

The second evaluation challenged MCNP6 to model a single source placed outside an edge of the box. This increased the straight-line distance required for an attenuated primary photon to penetrate the steel box. It also increased the factors associated with photons striking a face of the iron and scattering through it towards the detector. Observations were taken in a free field and shielded configuration, and the resulting GPFs are shown in Table 8.

Table 8. Experimental and MCNP Gamma Protection Factors for edge-centered sources outside the thick-assembly box.

Source	^{60}Co	^{137}Cs
Model GPF	2.89	4.47
Model GPF ±2σ	0.055	0.086
Experimental GPF	3.29	5.11
Experimental ±2σ	0.018	0.028

This "edge in" configuration significantly increased the GPFs for both ^{137}Cs and ^{60}Co. Although the straight-line path through the iron was only 40% greater than the face-centered configuration, the GPFs were approximately twice as high. This is likely due to the geometric factors associated with the setup. While nearly 50% of the photons from a face-centered source will strike the box, only 25% of an edge-centered source will strike the box. Additionally, all of the photons that do strike the panels will do so at or below an incident angle of 45 degrees, which increases their path length in the iron. The experimental GPFs were both higher than the MCNP6 models by 12%. It is likely that the aluminum frame, which lay on the straight-line path between the source and the detector, is a strong contributor to this discrepancy. The Mathematica peak attenuation model demonstrates that the aluminum frame should contribute a 3.01% GPF gain for ^{60}Co and a 4.27% GPF gain for ^{137}Cs peak photons. The shorter mean free paths of downscattered photons from the steel would likely drive this GPF up further. However, due to complications with the model geometry inputs, the frame was not simulated; this would be a good area for continued research.

The third evaluation placed the source outside a "point corner" of the box in an effort to further challenge its ability to handle three-dimensional photon transport. By

placing the source along a straight line from the center of the detector in the center of the box through a corner of the box, this evaluation maximized the straight-line distance required for an attenuated primary photon to penetrate the steel box and interact inside the detector. It also maximized the factors associated with photons striking a face of the iron and scattering through it towards the detector.

Table 9. Experimental and MCNP Gamma Protection Factors for sources outside the corner of the thick-assembly box.

Source	^{60}Co	^{137}Cs
Model GPF	4.28	8.96
Model GPF ±2σ	0.085	0.177
Experimental GPF	4.88	9.60
Experimental GPF ±2σ	0.043	0.090

The corner approach offered the best GPFs of the three configurations, shown in Table 9 to be approximately three times more than the face-centered configuration. This is due to geometric factors which reduce the number of photons incident upon the box. While almost half of the emitted photons in the face-centered configuration strike the box, slightly less than an eighth strike it in the corner-in configuration. Thus, fewer primary photons have a chance to scatter towards the detector, and most of those that do must pass through an increased thickness of iron due to their oblique incident angle to the panels of the iron box.

Again, the aluminum frame lay in the direct path between the source and the detector, so the experimental GPF was notably higher than the MCNP6 model. Interestingly, the degree to which the experimental GPF exceeded the model was by a

consistent 0.7. However, the proportional difference was 12% for the ^{60}Co and 6% for the ^{137}Cs, since the ^{137}Cs GPF was so significantly higher. Part of these discrepancies could be accounted for by the extra peak attenuation of the aluminum, which increased the attenuation by 5.27% for ^{137}Cs and 3.70% for ^{60}Co. However, the downscattered photons required the aluminum frame to be modeled in MCNP6, and the input deck was difficult to visualize with available software.

The final evaluation was designed to test MCNP6's ability to model multiple sources from multiple directions simultaneously. A ^{60}Co source was placed outside the corner of the box, while a ^{137}Cs source was placed at the center of an edge. Observations were taken in a free field and shielded configuration.
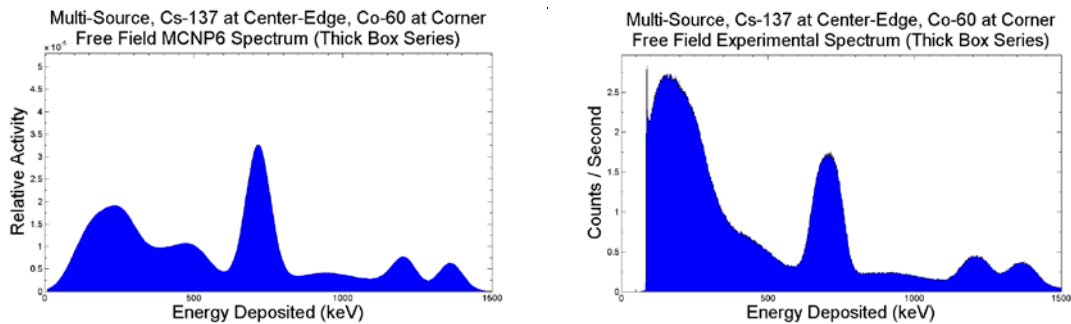
Figure 34. Comparison of free field MCNP6 simulation (left) and the corresponding experimental observation (right), for the thick-box, multi-source evaluation.
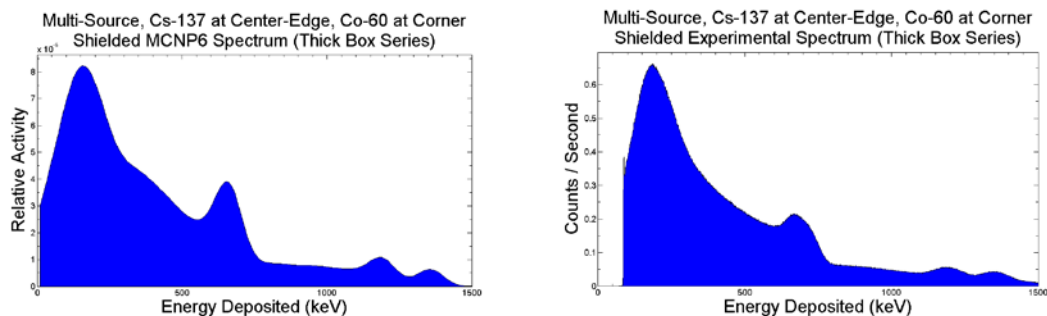
Figure 35. Comparison of shielded MCNP6 simulation (left) and the corresponding experimental observation (right), for the thick-box, multi-source evaluation.

75

Table 10. Gamma Protection Factors for Multi-Source Experiment and Model.

	GPF	2sigma
Experiment	**5.03**	**0.031**
Model	**4.6**	**0.101**

Using available reference data for the radioisotope sources, the current activities of the ^{137}Cs and ^{60}Co sources were calculated; these activities were then used to provide the appropriate probabilities of each peak in MCNP6. The resulting spectra were a very close match to MCNP6, as demonstrated in Figure 34 and Figure 35. Table 10 shows that the experimental GPF slightly exceeds the value of the model, most likely due to additional protection provided by the un-modeled aluminum frame.

5.9 Sources of Modeling Error

Although Section 5.9 addresses the statistical error for the work, there were many error sources that were difficult to quantify for both the model and the experiment. Most of these sources were assumed to have little impact.

While Section 5.5 explores the role of model fidelity, it does not evaluate a number of modeling assumptions and approximations. All MCNP6 models treated the sources as point sources, rather than as the round planchettes they are. The geometry of the room was either not included for thin assembly simulations or simplified to be a simple cube for the thick assembly simulations. The model included none of the other equipment in the room, including the table the box was on.

The steel box also had many simplifications. The box's aluminum frame and bolts were not included in the model, nor were the holes in the plates for the bolts and the detector cables. This likely drove the experimental GPF slightly higher, especially for experiments with sources outside the edges and corners. The thin assembly's plates overlapped at the corners, but this overlap was not modeled, since sources for this assembly were always placed at the center of a plate's face. The thick assembly's plates consisted of multiple powder-coated plates, and these coatings were not modeled, as they were assumed to be of insufficient mass to be significant contributors to gamma attenuation.

The detector was modeled as a single cylinder of NaI. The model did not include its aluminum sheath, photo-multiplier tube, or associated cables. The model also left out the aluminum stand which held the detector in the middle of the iron box.

The fidelity investigation of Section 5.5 suggests that these approximations likely had little effect on the overall work. If a back wall of the box can be removed with minimal effect, it follows that small holes or extra volumes made of low-mass gasses should also have a minimal effect.

5.10   Sources of Experimental Error

Low-level noise in the detector caused the greatest amount of experimental error. The upper limit for this noise varied depending on the source and shielding between 55 to 85 keV, and the low-level discriminator had to be adjusted to avoid having this noise flood the analog-digital converter with meaningless data. The likely cause of this low-level noise is fluorescence in the NaI which tends to build up and release over time from

the scintillator. As a result, none of the photons from 0 to approximately 80 keV were counted in the experiments. Since these photons tended to be shielded more effectively than the higher energy photons, this tended to drive the experimental GPFs down. However, since most of the actual dose came from higher-energy photons, this had a relatively small effect on the overall dose calculations and GPFs.

The high-voltage bias tended to fluctuate by approximately 20 V. Although the detector response function spread out peaks far more than these voltage fluctuations would do on their own, the fact remains that this likely contributed to the spreading. Future work could be improved by using a power regulation device.

When fully assembled with 1¼ inch walls, the bolts holding the box together were not a tight fit, nor were there enough bolts to fill every hole in every plate. The resulting mechanical play caused offsets of a few millimeters and gaps of up to a millimeter between adjacent plates. These imperfections had little influence on the overall experiment, but they could be a factor for future experiments with this box, particularly if a source is positioned so that it partly "shines through" one of these holes.

Finally, the dose calculations for the experimental measurements assumed a linear relationship between energy and bins for the NaI detector. Since the dose preferentially weights high-energy peaks, the highest-energy peak in each spectra determined the calibration of the entire spectrum. Although the detector's response is close to linear, these calculations could be more precise if they applied an interpolation between known calibration peaks.

6. Conclusions

6.1 Verifying MCNP6 Against Other Options

MCNP6 compares favorably to simplified-geometry simulations and GEANT4. The Mathematica model, the MATLAB Monte Carlo script, and GEANT4 were markedly slower and less portable. The custom Mathematica and MATLAB models could not approach the comprehensive particle simulation capabilities of MCNP6. While GEANT4 offered comparable capabilities, its higher input file complexity and slower computational time made it less suitable than MCNP6, and the spectrum it produced did not match the experimental results as closely as the spectrum produced by MCNP6. While other particle simulators might also suffice for this work, the comparisons performed in this research verify MCNP6 as an excellent platform for evaluating GPFs.

6.2 Validating MCNP6 to Produce Gamma Protection Factors

The models and experiments support MCNP6's validation for producing reliable GPFs. The program was able to produce both GPFs and spectra that closely matched experimental results despite significant simplifications and approximations in the model. The limits of this validation were not driven by MCNP6 or the available computing power, but rather the limitations of the detector systems used. The Germanium detector, while offering excellent spectral resolution, was inadequate for evaluating GPFs due energy efficiency factors unrelated to its photon-based material cross sections. The NaI detector was a far superior tool for GPF validation, though its performance below 75 keV reduced its utility for evaluating low-energy sources.

6.3 Examining Different Influences on Gamma Protection Factors

Varying the photon energies by using different radioisotopes showed a tendency towards high GPFs below 150 keV, even with relatively thin shielding. GPFs for photon sources at 662, 1173, and 1332 suggest a relatively flat region which corresponds to the dominance of the Compton scatter interaction. In this region, there is a GPF-neutral tradeoff between the lower attenuation of higher-energy photons and the tendency to scatter at wider angles for lower-energy photons.

The edge and corner studies in the thick-wall experiments suggest that shielding corners provide nearly as much protection as a flat plate with the same thickness as the path length through the corner. This is of particular interest for vehicles fielded during Operation Iraqi Freedom. The "V-shape" bottom of their hulls, created to deflect blast, should also offer improved protection from surface-deposited radioactive contamination directly underneath the vehicle. Similarly, this suggests that the sloped frontal armor of the Abrams tank should provide far better protection than its sides or back against the photon radiation burst of a nuclear weapon. In a civilian setting, a medical photon-based radiation treatment center might benefit from having its operator work from inside a shielded enclosure with the edge of the enclosure pointing toward the radiation source.

6.4 Future Work

The series of experiments on the thick-wall assembly suggest a relationship between wall thickness, peak energy, geometric configuration, and gamma protection factors that warrants further investigation. While the 73% increase in straight-line shielding associated with moving a source from the face of the box to the corner roughly corresponds to a proportional increase in its GPF, the proportionality varies with energy.

Characterizing this relationship would require a more extensive range of photon energies, and could suggest better shielding geometries against known sources and locations.

Another aspect of this problem that could produce some interesting results is evaluating the role of the detector's position within the armored enclosure. This would likely play a more significant role for penetrating photons that are prone to scattering at wider angles.

Although some of the models presented confirmed that MCNP6 uses characteristic X-rays and pair production in its photon transport, these mechanisms were not experimentally validated. Although the experimental spectra can validate the program's ability to model the Compton effect, these other mechanisms would require different sources and detectors.

The most important next step is to combine the work of this research with previous work in validating MCNP6 for neutron protection factors into a single radiation protection factor (RPF) validation in a single experiment and a single model. This could be evaluated using the fast burst reactor at White Sands Missile Range or a PuBe source at the Air Force Institute of Technology.

Bibliography

[1] X-5 Monte Carlo Team. *MCNP-A General Monte Carlo N-Particle Transport Code, Version 5, Volume I: Overview and Theory.* Los Alamos National Laboratory, 2003.

[2] Bridgman, Charles J. *Introduction to the Physics of Nuclear Weapons Effects.* Virginia: Defense Threat Reduction Agency, 2001.

[3] DTRA Public Affairs. *Operation TEAPOT Fact Sheet.* Defense Threat Reduction Agency, 2007.

[4] Decker, Andrew W. *Verification and Validation of Monte Carlo n-Particle Code 6 (MCNP6) with Neutron Protection Factor Measurements of an Iron Box.* Air Force Institute of Technology, 2014.

[5] Knoll, Glenn F.. *Radiation Detection and Measurement, 4th ed.* Wiley, 2010.

[6] Krane, K.S. *Introductory Nuclear Physics*. Wiley, 1988.

[7] Hubbel, J.H. and Seltzer, S.M. *Tables of X-Ray Mass Attenuation Coefficients and Mass Energy-Absorption Coefficients from 1 keV to 20 MeV for Elements Z = 1 to 92 and 48 Additional Substances of Dosimetric Interest.* National Institute of Standards and Technology, 1996. http://www.nist.gov/pml/data/xraycoef/.

[8] Weitze, Karen. "*AURORA PULSED RADIATION SIMULATOR*." Historic American Engineering Record, 2004. http://cryptome.org/eyeball/aurora/aurora-eyeball.htm

[9] Cember, H. *Introduction to Health Physics, 3rd ed*. McGraw-Hill, 1996.

[10] J. P. Raymond and E. L. Peterson, "Comparison of neutron, proton and gamma ray effects in semiconductor devices," IEEE Trans. Nucl. Sci., vol. NS-34, no. 6, pp. 1622–1628, Dec. 1987.

[11] S. Holinka, "Sun Sets on Sandia Pulsed Reactor," Sandia National Laboratories, Dec 2007. https://share.sandia.gov/news/resources/releases/2007/reactor.html

[12] Wolfram, "Mathematica Pricing: Mathematica for Government," viewed 20 November 2014,

http://www.wolfram.com/mathematica/pricing/government.php

[13] Blinder, S.M., "Klein-Nishina Formula for Compton Effect," Wolfram Demonstrations Project, 3 December, 2009,

http://demonstrations.wolfram.com/KleinNishinaFormulaForComptonEffect/

[14] Leung, J.K.C., "Application of Shielding Factors for Protection Against Gamma Radiations during a Nuclear Accident" IEEE Trans. Nucl. Sci., vol. 39, pp. 1512-1518, Oct. 1992.

[15] Charles N. Davidson, "Nuclear Notes Number 8: Armored Vehicle Shielding Against Radiation" US Army Nuclear and Chemical Agency, Fort Belvoir, VA, May 1979.

[16] Green, Taylor C, "Simulation of Reactor Pulses in Fast Burst and Externally Driven Nuclear Assemblies" ProQuest Dissertations And Theses; Thesis (Ph.D.)--The University of Texas at Austin, 2008.

[17] Stueker, Siegfried, "Calculation of Residual Radiation Protection afforded by the M113A1 Armored Personnel Carrier" US Army Armament Research and Development Command, Aberdeen Proving Ground, MD, Dec. 1978.

[18] Oliver, Mark A, "Army Pulse Radiation Facility (APRF) Gamma Dose Measurements" US Army Combat Systems Test Activity, Aberdeen Proving Ground, Md, Feb. 1993.

[19] Behrens, W. V., "The Effects of Short Duration Neutron Radiation on Semiconductor Devices" Diamond Ordnance Fuze Labs, IRE, March 1958.

[20] Cho, G., "Electronic Dose Conversion Technique Using a NaI(TI) Detector for Assessment of Exposure Dose Rate from Environmental Radiation" IEEE Transactions on Nuclear Science, Vol. 45, No. 3, Jun. 1998.

[21] Mathworks, "MATLAB Pricing and Licensing" viewed 10 January, 2015.

https://www.mathworks.com/pricing-

licensing/index.html?intendeduse=comm&s_tid=htb_learn_gtwy_cta1

[22] Shultis, J. K., "An MCNP Primer," Kansas State University, 2011.

www.nucleonica.net/wiki/images/6/6b/MCNPprimer.pdf

[23] Smith, S. W. "The Scientist and Engineer's Guide to Digital Signal Processing,"

California Technical Pub, 1997.

Appendix A: Experimental and MCNP6 Spectra

This appendix provides the experimental and modeled spectra taken. In most cases, the results are presented as side-by-side comparisons of experimental spectra and modeled spectra. The left side is the MCNP6 model spectrum, and the right side is the experimental spectrum.

Each figure is scaled to allow for a shape comparison between the model and experimental spectra. Unless otherwise noted, the modeled spectra have been convoluted with a point spread function to approximate the output of the detector system. All spectra were taken with the detector centered inside the steel enclosure.

Some results intended to study the characteristics of the MCNP6 model do not have corresponding experimental results.

Initial Validation

Initial validation spectra were taken with a ^{137}Cs source 14 inches away from the center of the detector. In the shielded configuration, the source was placed outside the center of one of the enclosure's steel plates.
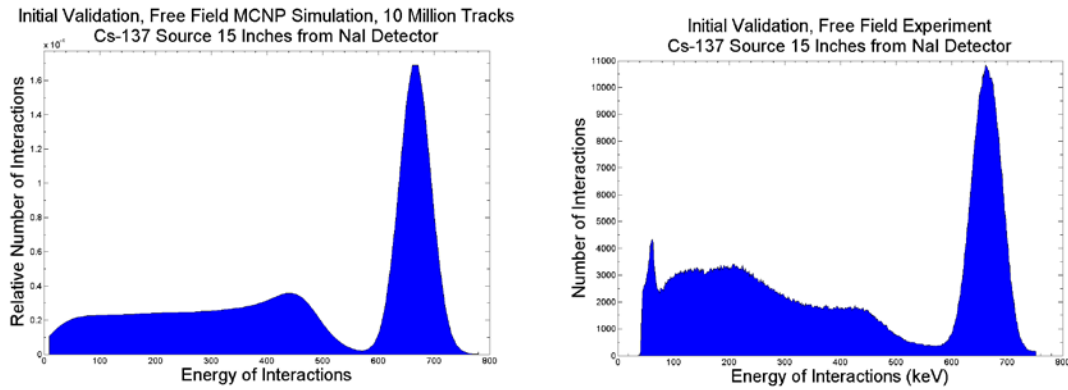
Figure 36. Initial validation, comparison of free field MCNP6 simulation (left) and the corresponding experimental observation (right).
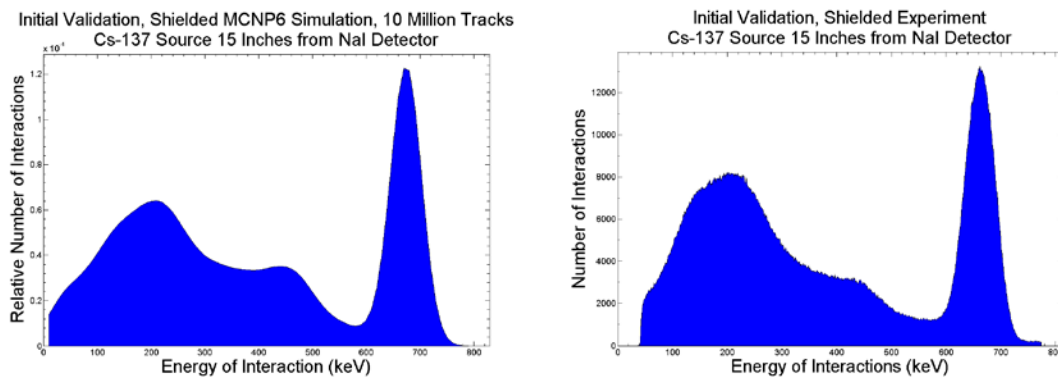
Figure 37. Initial validation, Initial validation with 1/4" steel walls, comparison of MCNP6 simulation (left) and the corresponding experimental observation (right).

Thin-Box Observations with Different Sources

The remainder of thin-box evaluations were set up identically to the initial validation experiment except for the sources. Different sources were used, though their placement was the same as the initial validation experiment, 14 inches from the detector, centered on the face of one of the enclosure's walls.

87

Figure 38. ^{60}Co source, comparison of free field MCNP6 simulation (left) and the corresponding experimental observation (right).

Figure 39. ^{60}Co source, comparison of shielded MCNP6 simulation (left) and the corresponding experimental observation (right).

Figure 40. ^{57}Co source, comparison of free field MCNP6 simulation (left) and the corresponding experimental observation (right).

Figure 41. ^{57}Co source, comparison of shielded MCNP6 simulation (left) and the corresponding experimental observation (right).

Figure 42. ^{109}Cd source, comparison of free field MCNP6 simulation (left) and the corresponding experimental observation (right).
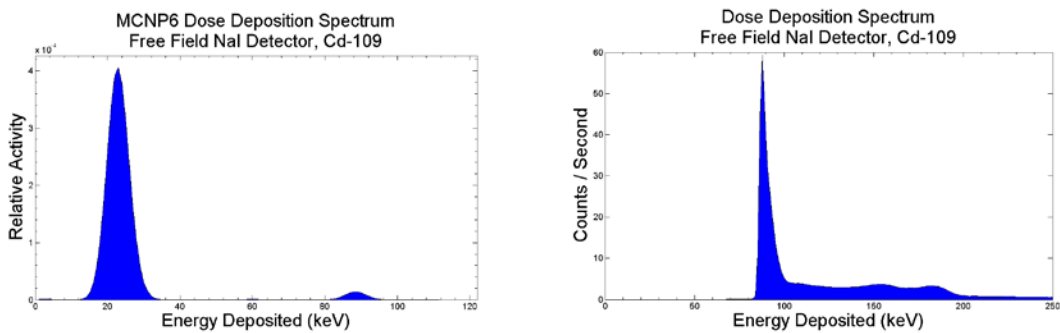
Figure 43. ^{109}Cd source, comparison of shielded MCNP6 simulation (left) and the corresponding experimental observation (right).

Fidelity Studies

Fidelity Studies were conducted in MCNP6 only and were not convoluted with any point spread functions.
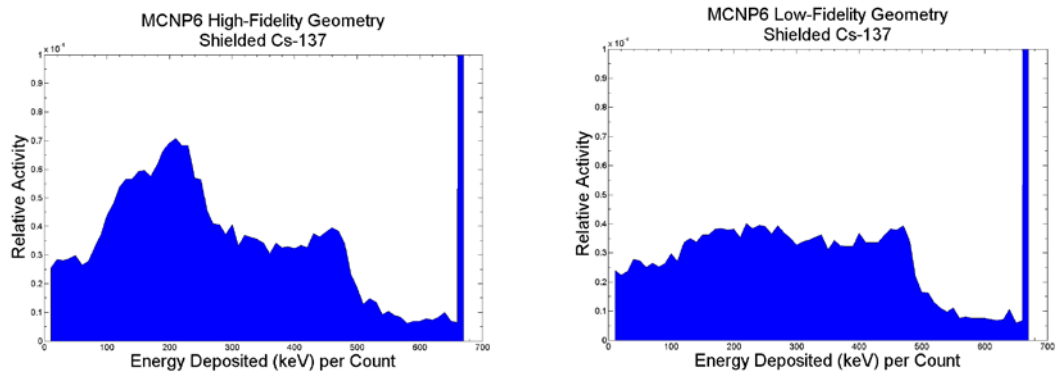
Figure 44. Comparison of high and low geometric fidelity spectra.
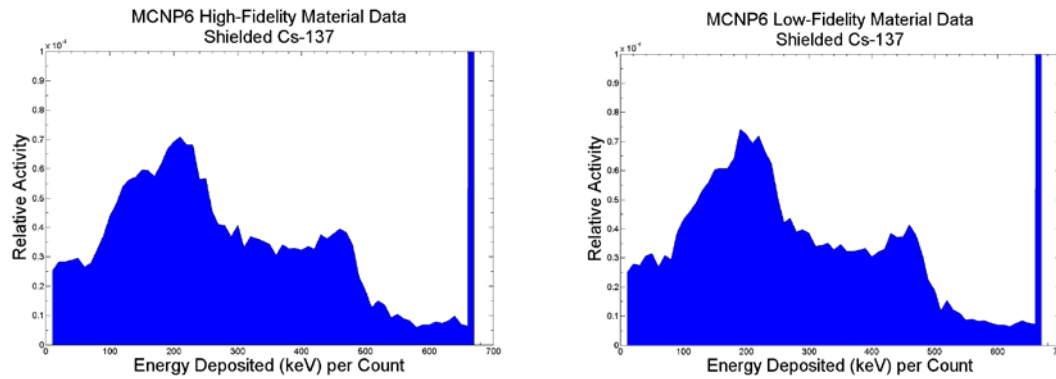
Figure 45. Comparison of high and low material data fidelity spectra.

Thick Box Observations

These observations were taken with the box in its full-thickness 1.25"
configuration using ^{137}Cs and ^{60}Co sources. The first series of observations and models
placed the source outside the center of one of the box's faces.

Figure 46. Comparison of free field MCNP6 simulation (left) and the corresponding experimental observation (right), for the thick-box, face-centered ^{137}Cs evaluation.

Figure 47. Comparison of shielded MCNP6 simulation (left) and the corresponding experimental observation (right), for the thick-box, face-centered ^{137}Cs evaluation.

Figure 48. Comparison of free field MCNP6 simulation (left) and the corresponding experimental observation (right), for the thick-box, face-centered ^{60}Co evaluation.

Figure 49. Comparison of shielded MCNP6 simulation (left) and the corresponding experimental observation (right), for the thick-box, face-centered ^{60}Co evaluation.

Edge-Centered Thick Box Observations

The second series of observations placed the source outside the edge. The sources were 14 inches away along the axis of the box's horizontal edges.

Figure 50. Comparison of free field MCNP6 simulation (left) and the corresponding experimental observation (right), for the thick-box, edge-centered ^{60}Co evaluation.

Figure 51. Comparison of shielded MCNP6 simulation (left) and the corresponding experimental observation (right), for the thick-box, edge-centered ^{137}Cs evaluation.

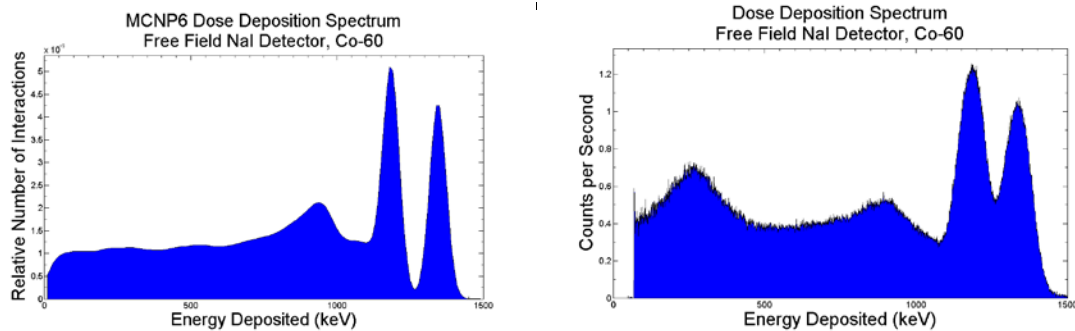**Figure 52. Comparison of free field MCNP6 simulation (left) and the corresponding experimental observation (right), for the thick-box, edge-centered ^{60}Co evaluation.**

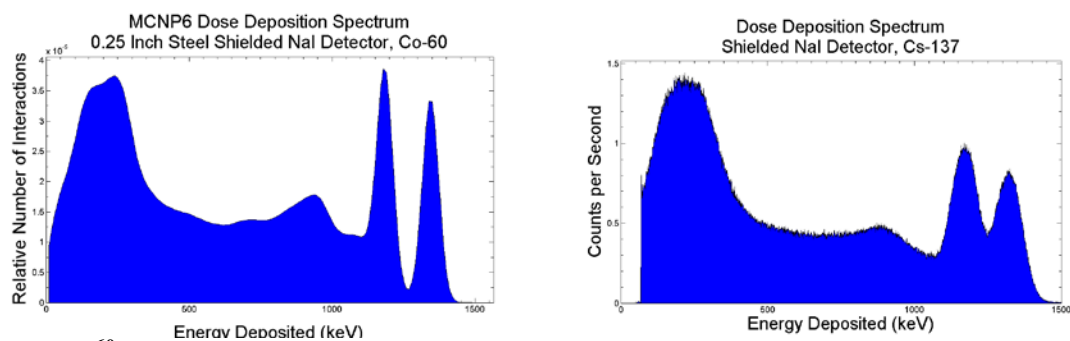**Figure 53. Comparison of shielded MCNP6 simulation (left) and the corresponding experimental observation (right), for the thick-box, edge-centered ^{60}Co evaluation.**

Corner Thick Box Observations

The third series of observations placed the source outside a corner of the box. The sources were placed 14 inches from the box's center along all three axes of the box's edges.
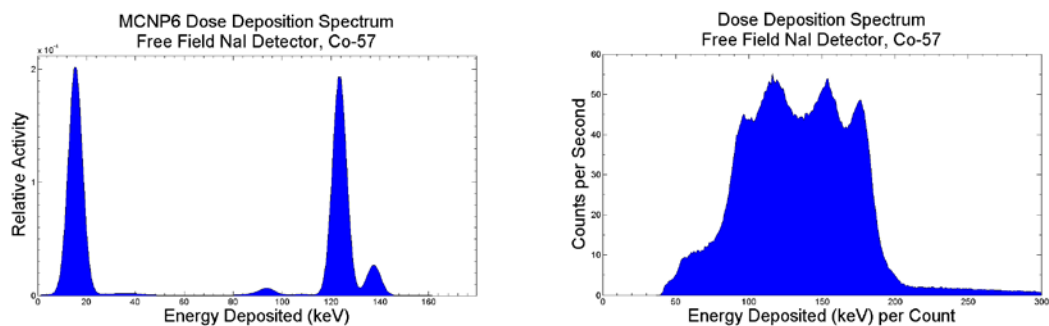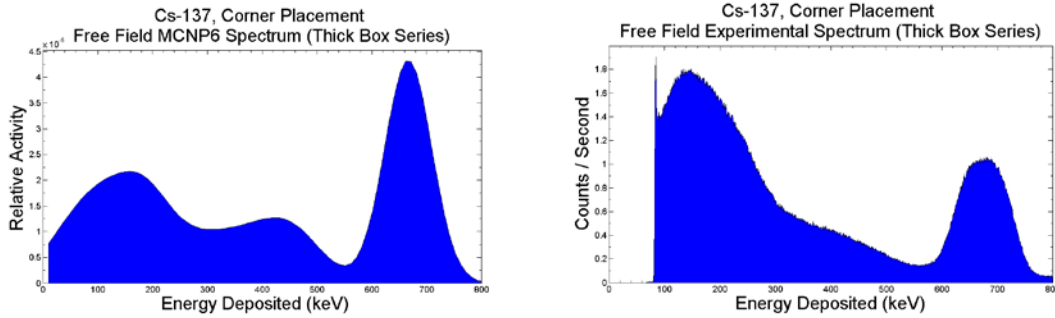

Figure 54. Comparison of free field MCNP6 simulation (left) and the corresponding experimental observation (right), for the thick-box, corner ^{137}Cs evaluation.
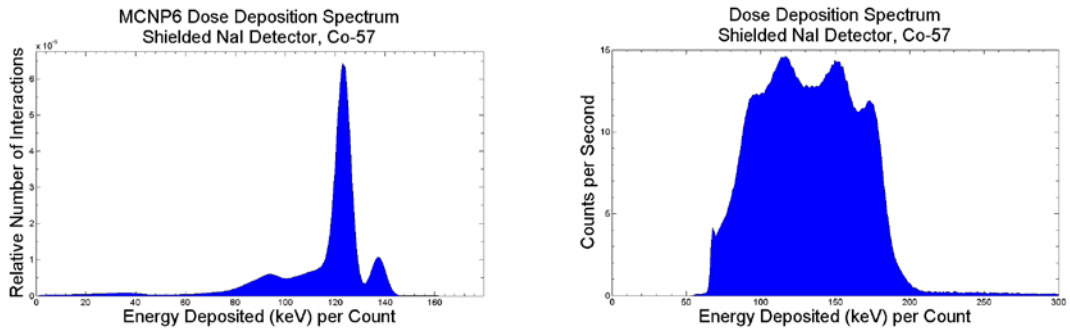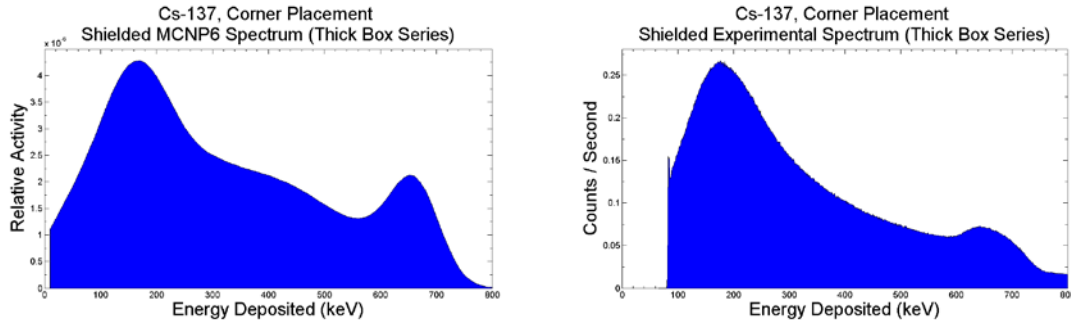

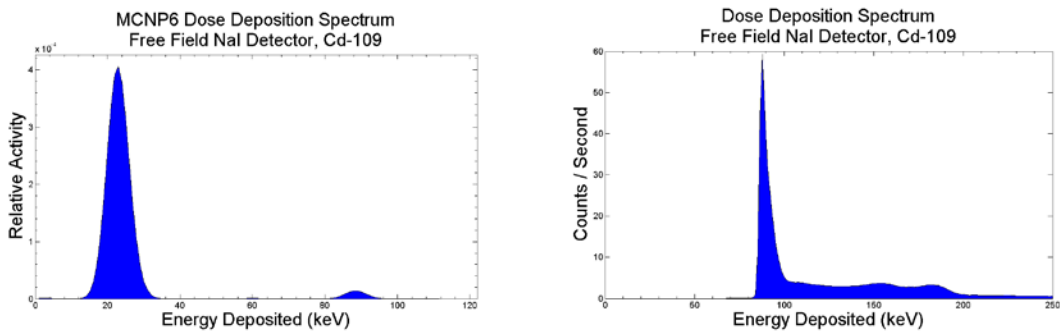**Figure 55. Comparison of shielded MCNP6 simulation (left) and the corresponding experimental observation (right), for the thick-box, corner ^{137}Cs evaluation.**
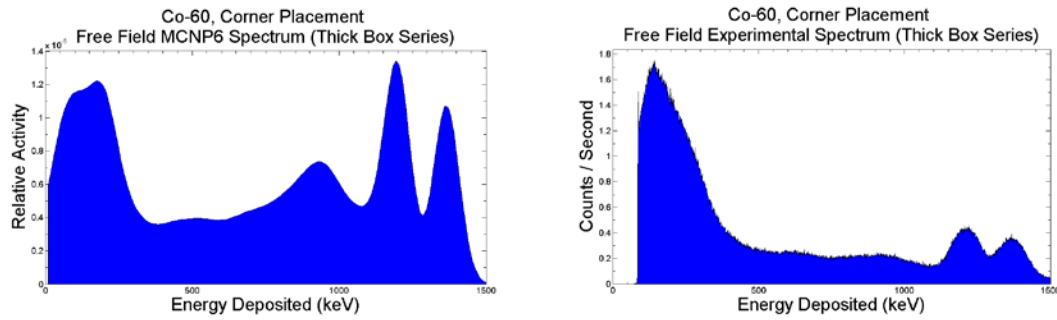
Figure 56. Comparison of free field MCNP6 simulation (left) and the corresponding experimental observation (right), for the thick-box, corner ^{137}Cs evaluation.
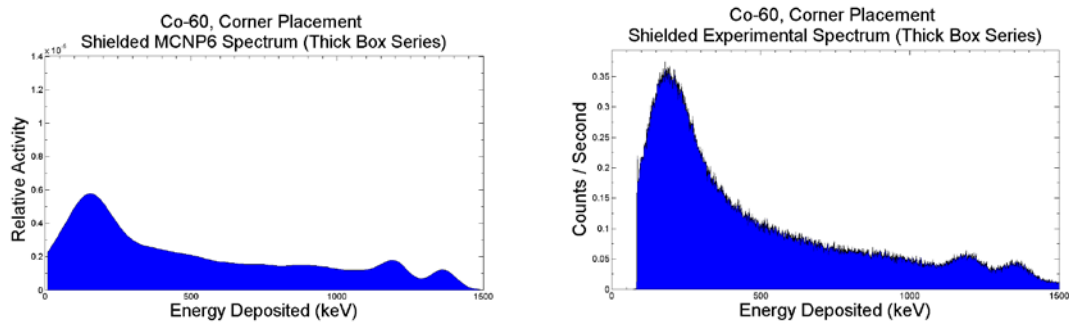
Figure 57. Comparison of shielded MCNP6 simulation (left) and the corresponding experimental observation (right), for the thick-box, corner ^{60}Co evaluation.

Multi-Source Observations

The final series of observations and models placed two sources in different locations outside the enclosure. The enclosure's walls for this observations were 1.25 inches thick. The ^{137}Cs was placed along the center of one edge, while the ^{60}Co outside a corner. These locations were identical to the earlier observations.
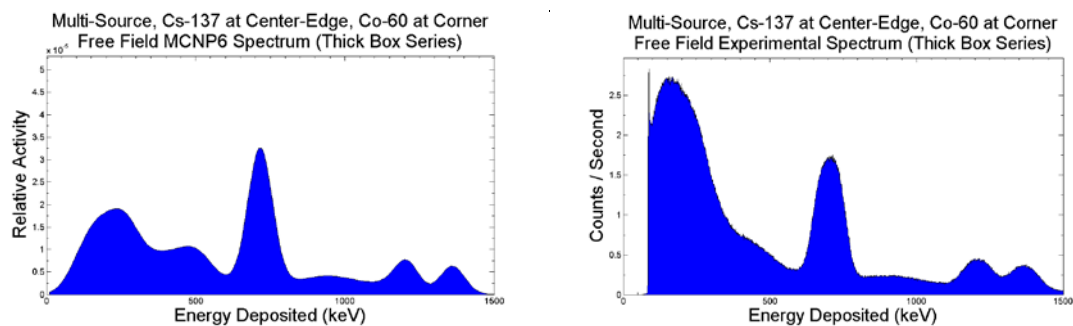
Figure 58. Comparison of free field MCNP6 simulation (left) and the corresponding experimental observation (right), for the thick-box, multi-source evaluation.

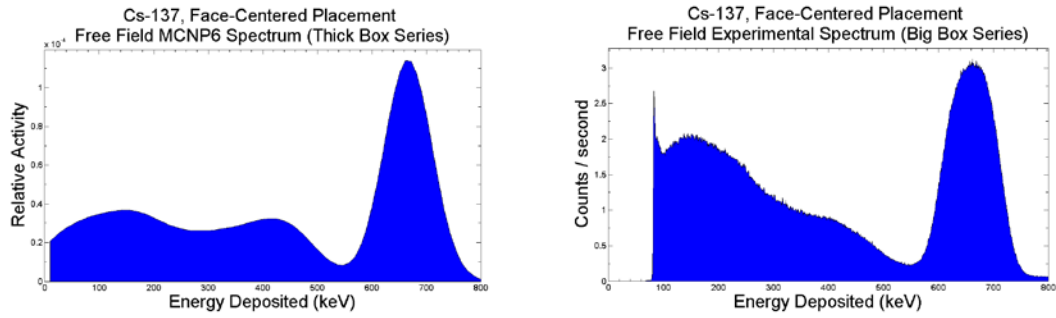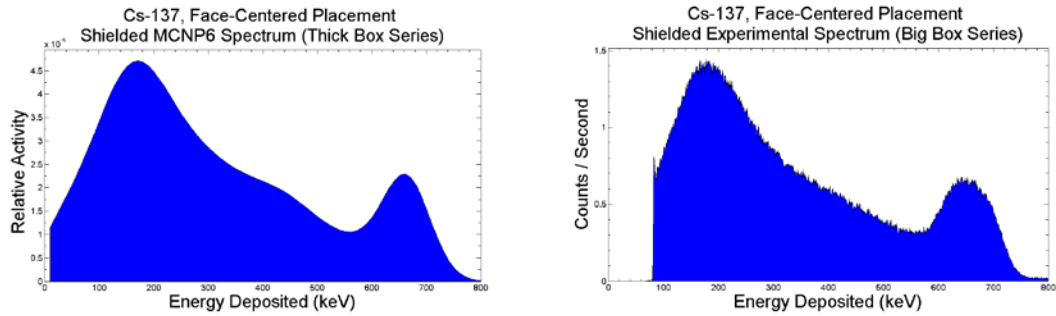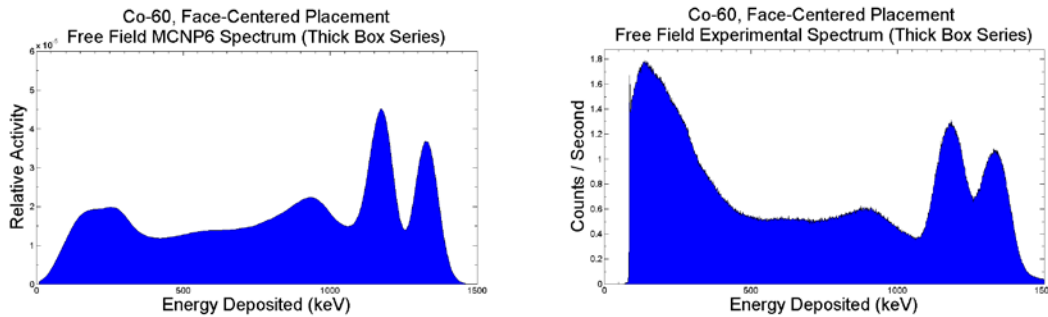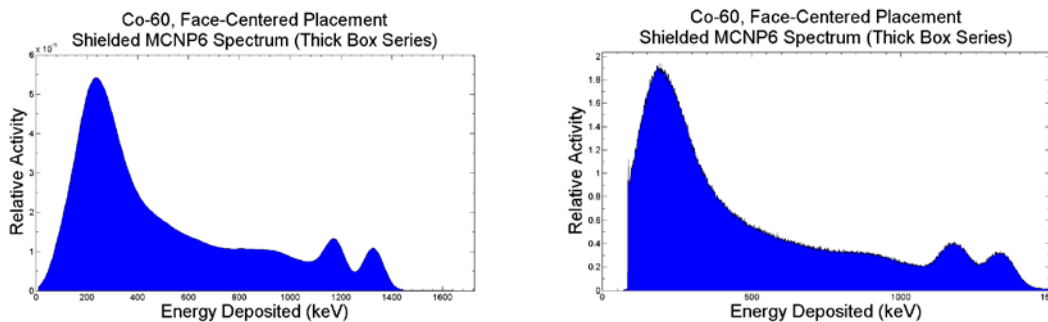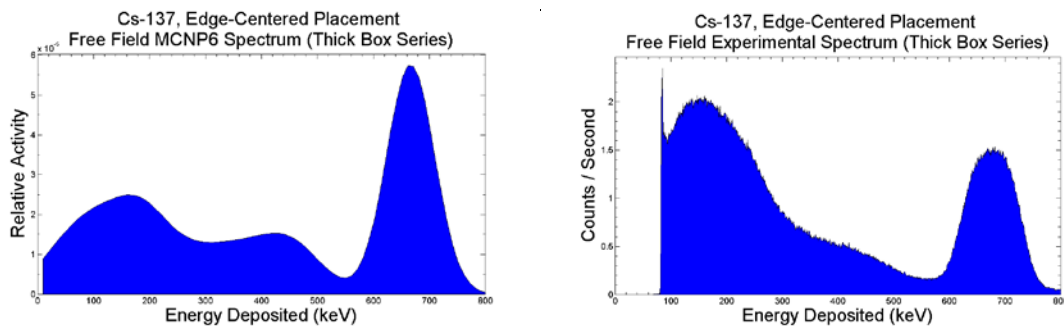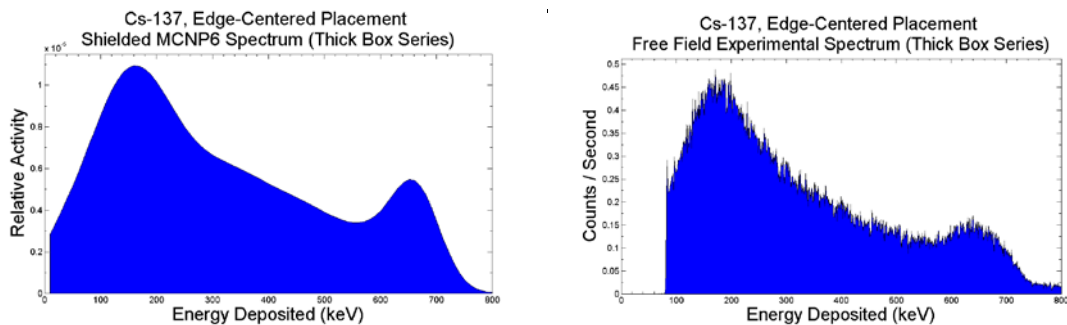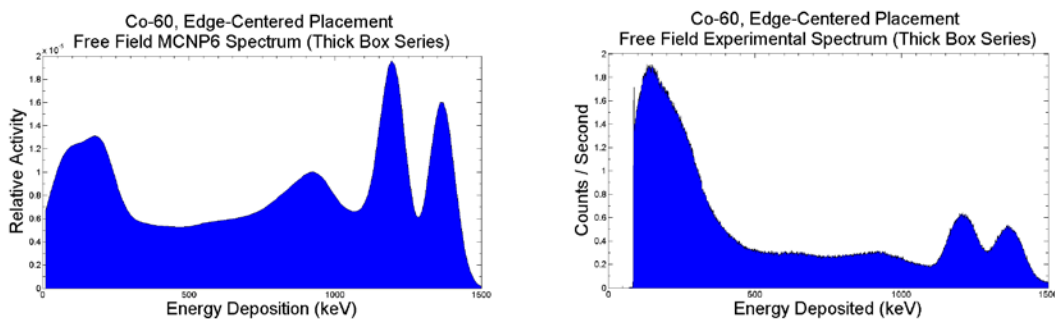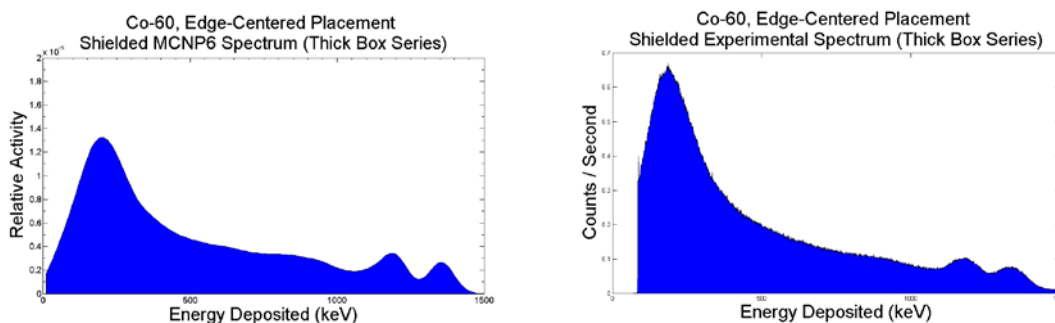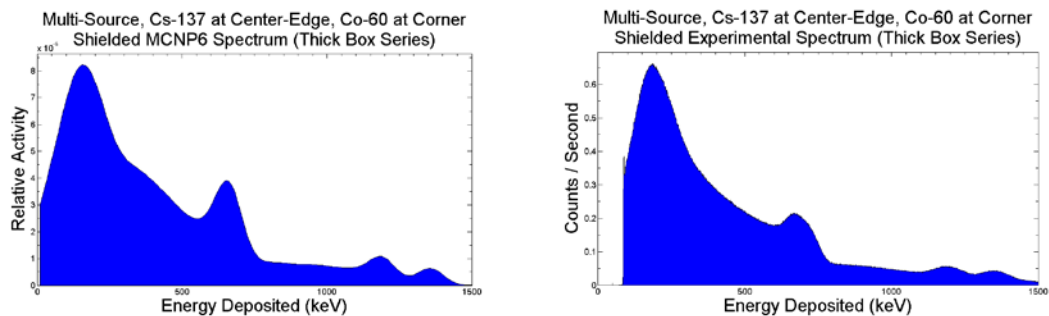**Figure 59. Comparison of shielded MCNP6 simulation (left) and the corresponding experimental observation (right), for the thick-box, multi-source evaluation.**

Appendix B: MCNP6 Input Files

This appendix presents and discusses three examples of the 30 MCNP6 input decks that produced the modeled spectra for this work. Each example illustrates key elements of a particular series of simulations.

Initial Validation

```
c cell cards
100   1    -0.001205  -10 20 30 40 50 60    imp:p=1  $ air in world (rpp)
200   2    -7.82      -20:-30:-40:-50:-60 70  imp:p=1  $ iron shield (lots of rpp's)   1    -0.001205
300   1    -0.001205  -70 80               imp:p=1  $ air in shielded box
400   3    -3.67      -80                  imp:p=1  $ NaI detector
999   0               10                   imp:p=0  $ rest of the world


c surface cards
10   rpp  0      255.88 0      255.88 0      255.88                $ problem bounding surface
20   rpp  99.365 156.515 99.365 156.515 99.365 156.515  $ steel box cube
30   rpp  97.46  158.42  97.46  158.42  155.88 156.515      $ steel box lid
40   rpp  97.46  158.42  97.46  158.42  99.365 100          $ steel box base
50   rpp  97.46  158.42  99.365 100     99.365 156.515      $ steel box left side
60   rpp  97.46  158.42  155.88 156.515 99.365 156.515      $ steel box right side
70   rpp  100    155.88  100    155.88 100    155.88            $ air inside the box
80   rcc  127.94 127.94 124.13 0 0 7.62 3.81                    $ NaI Detector, cylinder


c material specification
m1   07014 0.8   8016 0.2                              $ air
m2   26000 0.977170  6012  0.022831             $ shield, carbon steel
m3   11023 -0.5   53127 -0.5                     $ Sodium Iodide
mode p
SDEF POS=90 127.94 127.94 PAR=p ERG=.662        $ source position, type, energy photons of energy
.6617 MeV
nps  1000000                                     $ number of photons generated
f8:p 400                                         $ Energy deposition in detector
E8   0 1.e-5 .01 .02 .03 .04 .05 .06 .07 .08 .09 &     $ Energy bins for the spectrum in 10keV increments
   .1 .11 .12 .13 .14 .15 .16 .17 .18 .19 .20 .21 .22 .23 .24 .25 &
   .26 .27 .28 .29 &
   .30 .31 .32 .33 .34 .35 .36 .37 .38 .39 &
   .40 .41 .42 .43 .44 .45 .46 .47 .48 .49 &
   .50 .51 .52 .53 .54 .55 .56 .57 .58 .59 &
   .60 .61 .62 .63 .64 .65 .66 .662
```

The shielded and unshielded input decks are nearly identical, and this remained true for all subsequent simulations that produced a GPF. Swapping the highlighted portions changed the "box cell" material and density from air to iron. This technique is effectively an on/off switch for the simulation's shield for every simulated GPF produced.

Alternate Source Study

```
c cell cards
100   1    -0.001205  -10 20              imp:p=1          $ air in world (rpp)
```

```
200   1    -0.001205  -20 70          imp:p=1        $ iron shield (lots of rpp's)  2    -7.82
300   1    -0.001205  -70 80          imp:p=1        $ air in shielded box
400   3    -3.67      -80             imp:p=1         $ HPGe detector
999   0              10              imp:p=0          $ rest of the world

c surface cards
10  rpp  0     255.88 0     255.88 0     255.88              $ problem bounding surface
20  rpp  99.365 156.515 99.365 156.515 99.365  156.515  $ steel box cube
70  rpp  100    155.88  100    155.88 100     155.88         $ air inside the box
80  rcc  127.94 127.94 123.525 0 0 8.83 3.15                $ NaI Detector, cylinder

c material specification
m1   07014 0.8  8016 0.2                               $ air
m2   26000 0.977170  6012  0.022831              $ shield, carbon steel
m3   11023 -0.5   53127 -0.5                          $ Sodium Iodide
mode p
SDEF POS=92.38 127.94 127.94 PAR=p ERG=D1  $ source position, type, energy
SI1  L 1.173 1.332
SP1    1.0  1.0
nps  10000000                              $ number of photons generated
f8:p 400                                    $ Energy deposition in detector
e8   0 1.e-5 &
       0.01 0.02 0.03 0.04 0.05 0.06 0.07 0.08 0.09 &
     0.10 0.11 0.12 0.13 0.14 0.15 0.16 0.17 0.18 0.19 &
     0.20 0.21 0.22 0.23 0.24 0.25 0.26 0.27 0.28 0.29 &
     0.30 0.31 0.32 0.33 0.34 0.35 0.36 0.37 0.38 0.39 &
     0.40 0.41 0.42 0.43 0.44 0.45 0.46 0.47 0.48 0.49 &
     0.50 0.51 0.52 0.53 0.54 0.55 0.56 0.57 0.58 0.59 &
     0.60 0.61 0.62 0.63 0.64 0.65 0.66 0.67 0.68 0.69 &
     0.70 0.71 0.72 0.73 0.74 0.75 0.76 0.77 0.78 0.79 &
     0.80 0.81 0.82 0.83 0.84 0.85 0.86 0.87 0.88 0.89 &
     0.90 0.91 0.92 0.93 0.94 0.95 0.96 0.97 0.98 0.99 &
     1.00 1.01 1.02 1.03 1.04 1.05 1.06 1.07 1.08 1.09 &
     1.10 1.11 1.12 1.13 1.14 1.15 1.16 1.17 1.18 1.19 &
     1.20 1.21 1.22 1.23 1.24 1.25 1.26 1.27 1.28 1.29 &
     1.30 1.31 1.32 1.33 1.34
```

This series of simulations varied the sources to simulate the emission spectra of ^{60}Co, ^{57}Co, and ^{109}Cd. All sources were simulated as point sources. The highlighted portion is the section varied to produce the appropriate source emissions, which in this case matches the energies and relative activities of ^{60}Co.

Thick Wall Assembly
```
c cell cards
100   1    -0.001205  -30 20          imp:p=1        $ air in room (rpp)
200   2    -7.874     -20 70          imp:p=1        $ iron shield (rpp)    2    -7.874
300   1    -0.001205  -70 80          imp:p=1         $ air in shielded box
400   3    -3.67      -80             imp:p=1        $ NaI detector
500   4    -2.4       -10 30          imp:p=1        $ Concrete floor, walls, and ceiling
999   0              10              imp:p=0        $ rest of the world

c surface cards
```

```
10   rpp   -100 355.88   -100 355.88   -100 355.88          $ problem bounding surface
20   rpp   96.825 159.055 96.825 159.055 96.825  159.055   $ Outer Steel Surface
30   rpp   0      255.88  0      255.88  0      255.88      $ Inner surface of concrete enclosure
70   rpp   100    155.88  100    155.88  100    155.88      $ Inner steel surface
80   rcc   127.94 127.94 124.13 0 0 7.62 3.81              $ NaI Detector, cylinder

c material specification
m1   07014 0.778   07015 0.00286 &
     8016  0.20896 8017 0.000817  8018  0.000421 &
     18040 0.00930 18036 0.000315  18038 0.00005884          $ air
m2   26056 0.896   26054 0.0567  &
     26057 0.0215 26058 0.00274 &
     6012  0.0226  6013  0.000251                            $ shield, carbon steel
m3   11023 -0.5    53127 -0.5                                $ Sodium Iodide
m4   1001 -0.01    6012 -0.001   8016 -.529107 &
     11023 -0.002  12024 -0.002  13027 -0.033872 &
     14028 -0.337021 19039 -0.013 20040 -0.044 &
     26000 -0.14000                                          $Concrete
mode p
sdef x=92.38 y=92.38 z=D20
     erg=FZ=D45                         $Position and energy
si20 L 127.94 163.5 163.5              $ Discrete Z coordinates for point sources
sp20 254.8685 147.7268 147.7268        $ Relative Probability
ds45 L 0.662 1.173 1.332               $ Energies in MeV
nps  10000000                          $ number of photons generated
f8:p 400                               $ Energy deposition in detector
e8   0 1.e-5 &
     0.01 0.02 0.03 0.04 0.05 0.06 0.07 0.08 0.09 &
     0.10 0.11 0.12 0.13 0.14 0.15 0.16 0.17 0.18 0.19 &
     0.20 0.21 0.22 0.23 0.24 0.25 0.26 0.27 0.28 0.29 &
     0.30 0.31 0.32 0.33 0.34 0.35 0.36 0.37 0.38 0.39 &
     0.40 0.41 0.42 0.43 0.44 0.45 0.46 0.47 0.48 0.49 &
     0.50 0.51 0.52 0.53 0.54 0.55 0.56 0.57 0.58 0.59 &
     0.60 0.61 0.62 0.63 0.64 0.65 0.66 0.67 0.68 0.69 &
     0.70 0.71 0.72 0.73 0.74 0.75 0.76 0.77 0.78 0.79 &
     0.80 0.81 0.82 0.83 0.84 0.85 0.86 0.87 0.88 0.89 &
     0.90 0.91 0.92 0.93 0.94 0.95 0.96 0.97 0.98 0.99 &
     1.00 1.01 1.02 1.03 1.04 1.05 1.06 1.07 1.08 1.09 &
     1.10 1.11 1.12 1.13 1.14 1.15 1.16 1.17 1.18 1.19 &
     1.20 1.21 1.22 1.23 1.24 1.25 1.26 1.27 1.28 1.29 &
     1.30 1.31 1.32 1.33 1.34
```

This series of simulations increased the thickness of the steel enclosure to 1.25". It also defines a small concrete room around the box. The location of the source was then varied, and the type of source was interchanged between ^{137}Cs and C0-60. This particular example is the multi-source configuration, which has both types of sources: [137]Cs outside an edge, and ^{60}Co outside a corner.

Fidelity Study
The example above also shows some of the variations that came from the fidelity study. This series of simulations varied the material data cards, the number of particles in the source card, and the surface and cell cards defining the geometry. One noteworthy

difference in the example provided is the complexity of the material data cards, which include more elements and isotopes than the earlier series of models.

Appendix C: MATLAB Monte Carlo Script

```
%This is the Monte Carlo code for transporting monoenergetic photons from
%a point source to a detector between two iron barrier.

clear all
clc

%This simulation tracks photons as they Compton scatter through a slab
%geometry configuration to represent a point source .

%INPUTS
%To change the setup, you should alter the following variables
tracks=10000000;          %Number of primary photon tracks to be evaluated.
primeenergy=.662;        %Primary photon energy in MeV, from .001 to 20


%------------------------------------------------------------------------
%SURFACE LOCATION INPUTS
%Below is a crude diagram of the setup showing where each surface boundary
%is located. These boundaries can be changed, but be careful!
%Each boundary must be given a coordinate relative to the other boundaries
%All coordinates are in cm.

% negair    src    nio   nii     NaIpos     fii    fio
%
% |        s      | iron |       NaI        | iron |
% |        s      | iron |       NaI        | iron |
% |        s      | iron |       NaI        | iron |
% |    air   s  air  | iron |  air   NaI    air  | iron |
% |        s      | iron |       NaI        | iron |
% |        s      | iron |       NaI        | iron |
% |        s      | iron |       NaI        | iron |

src = 0; %position of the source
negair= -100; %left boundary of the simulation, must be negative.
nio = 10; %outer surface of the near iron barrier, must be positive.
nii = 11; %inner surface of the near iron barrier, must be greater than nio.
NaIpos = 41.5; %position of center of the NaI detector.
fii =  70; %inner surface of the far iron barrier, must be greater than fNaI.
fio = 71;  %outer surface of the far iron barrier and far boundary of the
       %simulation, must be the highest of these coords.
%---------------------------------------------------------------------------


%We begin by defining variables that will endure throughout the simulation.

DetectorPosition=10000; %This shows a position for evaluating the flux.
Energydata=zeros(1, (tracks/2)); %Initialize what will be an allocatable array. This will
        %provide the photon flux output of the Monte Carlo simulation.
n=1;    %This is a counter for the number of photons that pass through the
     %detector's coordinate.
%
%Now we input the NIST data tables
AirEnergies = [1.00000E-03, 1.50000E-03,2.00000E-03,3.00000E-03, 3.20290E-03, 3.202901E-
03,4.00000E-03,5.00000E-03,6.00000E-03,8.00000E-03,1.00000E-02,1.50000E-02,2.00000E-02,3.00000E-
02,4.00000E-02,5.00000E-02,6.00000E-02,8.00000E-02,1.00000E-01,1.50000E-01,2.00000E-01,3.00000E-
```

01,4.00000E-01,5.00000E-01,6.00000E-01,8.00000E-
01,1.00000E+00,1.25000E+00,1.50000E+00,2.00000E+00,3.00000E+00,4.00000E+00,5.00000E+00,6.00000E+00,8.00000E+00,1.00000E+01,1.50000E+01,2.00000E+01];
AirCoefficients=
[3.606E+03,1.191E+03,5.279E+02,1.625E+02,1.340E+02,1.485E+02,7.788E+01,4.027E+01,2.341E+01,9.921E+00,5.120E+00,1.614E+00,7.779E-01,3.538E-01,2.485E-01,2.080E-01,1.875E-01,1.662E-01,1.541E-01,1.356E-01,1.233E-01,1.067E-01,9.549E-02,8.712E-02,8.055E-02,7.074E-02,6.358E-02,5.687E-02,5.175E-02,4.447E-02,3.581E-02,3.079E-02,2.751E-02,2.522E-02,2.225E-02,2.045E-02,1.810E-02,1.705E-02];
IronEnergies = [.001, 1.5*10^-3, 2*10^-3, 3*10^-3, 4*10^-3, 5*10^-3, 6*10^-3, 7.111*10^-3, 7.112*10^-3, 8*10^-3, 10*10^-3, 15*10^-3, 20*10^-3, 30*10^-3, 40*10^-3, 50*10^-3, 60*10^-3, 80*10^-3, 100*10^-3, 150*10^-3, 200*10^-3, 300*10^-3, 400*10^-3, 500*10^-3, 600*10^-3, 800*10^-3, 1000*10^-3, 1250*10^-3, 1500*10^-3, 2000*10^-3, 3000*10^-3, 4000*10^-3, 5000*10^-3, 6000*10^-3, 8000*10^-3, 10000*10^-3, 15000*10^-3, 20000*10^-3];
IronCoefficients = [9.085*10^2*10, 399*10^2*10, 1.626*10^2*10, 5.576*10^1*10, 2.567*10^1*10, 1.398*10^1*10, 8.484*10, 5.319*10, 4.076*10^1*10, 3.056*10^1*10, 1.076*10^1*10, 5.708*10, 2.568*10, 8.176*10^-1*10, 3.629*10^-1*10, 1.958*10^-1*10, 1.205*10^-1*10, 5.952*10^-2*10, 3.717*10^-2*10, 1.964*10^-2*10, 1.460*10^-2*10, 1.099*10^-2*10, 9.4*10^-3*10, 8.414*10^-3*10, 7.704*10^-3*10, 6.699*10^-3*10, 5.995*10^-3*10, 5.350*10^-3*10, 4.883*10^-3*10, 4.265*10^-3*10, 3.621*10^-3*10, 3.312*10^-3*10, 3.146*10^-3*10, 3.057*10^-3*10, 2.991*10^-3*10, 2.994*10^-3*10, 3.092*10^-3*10, 3.224*10^-3*10];

denair=.0012922;   %density of air, in grams/cm^3
deniron = 7.874;   %density of iron, in grams/cm^3

%The Monte Carlo program is governed by a for loop that starts a primary
%photon and runs it through a set number of tracks. These tracks continue
%through multiple interactions until a kill criteria is met, at which point
%a new primary photon is
%created.
for i = 1:tracks
location = src;   %This is the source location, which can be moved, in cm.
energy = primeenergy;
angle = pi*rand(1); %Initial angle of the photon with respect to the
                %plane of the iron barrier.

while (negair <= location <= fio) %This is the primary loop that drives each track
                %It will keep running as long as
                %the photon remains

mfp=(-log(1-rand(1)))/(log(2)); %Samples the number of mean free paths
                    %a particle will travel before interacting

%--
%This section produces the mean free path length for air, iron, and NaI
%for the current energy of the photon. This uses a log-log interpolation of
%NIST data for air, iron, sodium, and iodine.

% We start with two lists of photon energies and attenuation constants
%from NIST.
k=length(AirEnergies);
while k >= 1   %This finds the NIST entry just below the
  if (AirEnergies(k) > energy) %energy of the photon.
    k = k-1;
  else
    break
  end

```
end
%Now we do the log-log interpolation.
lair = log(AirCoefficients(k)) * (log(AirEnergies(k+1)) - log(energy)) / (log(AirEnergies(k+1)) -
log(AirEnergies(k))) + log(AirCoefficients(k+1)) * (log(energy) - log(AirEnergies(k))) /
(log(AirEnergies(k+1)) - log(AirEnergies(k)));
airAtten=exp(lair);   %This is the cross section per density, cm^2 per gram
pathAir=(-log(0.5))/((airAtten)*denair);

%Now we repeat the same process for iron.
k=length(IronEnergies);
while k >= 1              %This finds the NIST entry just below the
   if (IronEnergies(k) > energy) %energy of the photon.
      k = k-1;
   else
      break
   end
end
%Now we do the log-log interpolation.
liron = log(IronCoefficients(k)) * (log(IronEnergies(k+1)) - log(energy)) / (log(IronEnergies(k+1)) -
log(IronEnergies(k))) + log(IronCoefficients(k+1)) * (log(energy) - log(IronEnergies(k))) /
(log(IronEnergies(k+1)) - log(IronEnergies(k)));
ironAtten=exp(liron);   %This is the cross section per density, cm^2 per gram
pathIron=(-log(0.5))/((ironAtten)*deniron);

%----------------------------------------------------------------------------
%This section transports the photon along its trajectory until its number
%of mean free paths has been reduced to zero.


previouslocation=location; %This stows the starting location for use later.

while mfp > 0 %This loop will transport the photon left or right as necessary through the surfaces of the
problem.

   if location <= nio %This is the outer air loop. It identifies if the photon is currently in the air outside
the box and transports it.
      if ((mfp*pathAir*cos(angle))+location) >= nio; %If it moves out of the air and into the near iron
barrier
         mfp=mfp-(((nio-location)/(pathAir*cos(angle)))); % reduces mfp appropriately
         location = nio; %Now it's out of the air and ready for the near iron barrier loop.
      else
         location = location + mfp*pathAir*cos(angle); %shows where the next interaction happens if it
starts and ends in the outer air.
         mfp=0;
      end
   end

   if nii>=location
      if location >=nio % These if statements identify if the photon is currently inside the near iron
barrier
         if ((mfp*pathIron*cos(angle))+location) >= nii; %If it moves into the air inside the box
            mfp=mfp-(((nii-location)/(pathIron*cos(angle)))); % reduces mfp appropriately
            location = nii; %Now it's at the inner iron surface, ready for the inner air loop.
         elseif((mfp*pathIron*cos(angle))+location) <= nio; %If it moves into the air outside the box
            mfp=mfp-abs((((location-nio)/(pathIron*cos(angle))))); % reduces mfp appropriately
            location = nio; %Now it's outside the box, ready for the outer air loop.
         else
            location = location + mfp*pathIron*cos(angle); %shows where the next interaction happens if
the beginning and end are in the air.
            mfp=0;
```

```
        end
      end
    end

  if fii>=location
      if location >=nii % These if statements identify if the photon is currently in the 'inner air' between
the iron barriers
          if ((mfp*pathAir*cos(angle))+location) >= fii; %If it moves into the far barrier
              mfp=mfp-(((fii-location)/(pathAir*cos(angle)))); % reduces mfp appropriately
              location = fii; %Now it's at the inner iron surface, ready for the far iron loop.
          elseif((mfp*pathAir*cos(angle))+location) <= nii; %If it moves into near iron barrier
              mfp=mfp-abs((((location-nii)/(pathAir*cos(angle))))); % reduces mfp appropriately
              location = nii; %Now it's outside the box, ready for the outer air loop.
          else
              location = location + mfp*pathAir*cos(angle); %shows where the next interaction happens if
the beginning and end are in the air.
              mfp=0;
          end
      end
  end

  if fio>=location
      if location >=fii % These if statements identify if the photon is currently inside the far iron barrier
          if ((mfp*pathIron*cos(angle))+location) <= fii; %If it moves into the air inside the box
              mfp=mfp-abs((((location-fii)/(pathIron*cos(angle))))); % reduces mfp appropriately
              location = fii; %Now it's out of the iron and ready for the inner air loop.
      else
              location = location + mfp*pathIron*cos(angle); %shows where the next interaction happens if
the beginning and end are in the iron.
              mfp=0;
          end

      end
  end

end
%------------------------------------------------------------------
%The photon is now at its interaction location. Now we run our kill criteria.
if (location) < negair %This is a kill criteria. any photon that makes it a meter away from the source in
the wrong direction is killed.
    break
end

if (location) > fio %This is a kill criteria. any photon that makes it through the far side iron barrier is
killed.
    break
end
%------------------------------------------------------------------
%Now we must determine if the photon passed through the plane of interest.
if previouslocation <= NaIpos  %Checks to see if the photon has crossed the altitude of interest from left
to right
    if location > NaIpos
      Energydata(n)=energy;  %adds the photon energyto the altitude of interest.
      n=n+1;
    end
end

if previouslocation >= NaIpos %Checks to see if the photon has crossed the altitude of interest from
right to left
    if location < NaIpos
```

```
        Energydata(n)=energy;  %adds the photon energyto the altitude of interest.  %adds the photon
energy
        %to the altitude of interest.
        n=n+1;
    end
end
%-----------------------------------------------------------
% The following section establishes and samples from
%the Klein Nishina distribution. I use rejection sampling for this.
sample = 0;
gamma=energy/.511;
while sample < 1
    fcompmax = energy/(1+gamma*(1-cos(0)));
    knprobmax = (1/2)*((fcompmax)^2)*(1+(cos(0))^2+((((gamma)^2)*((1-cos(0))^2))/(1+gamma*(1-
cos(0)))));
    %(1/2)*((fcompmax)^2)*(fcompmax+((fcompmax)^(-1))-((sin(fcompmax))^2)); %Normalizes the
probability distribution.
    knsample=pi*rand(1);
    fcomp = energy/(1+(gamma)*(1-cos(knsample)));
    knprob = (1/2)*((fcomp)^2)*(1+(cos(knsample))^2+((((gamma)^2)*((1-
cos(knsample))^2))/(1+gamma*(1-cos(knsample)))));
    %(1/2)*((fcomp)^2)*(fcomp+((fcomp)^(-1))-((sin(knsample))^2));

    if rand(1)<=(knprob/knprobmax) %
        scatterangle=knsample;
        sample=2; %The sample is accepted, this value kills the while loop.
    end
end


%-------------------------------------------------------
if energy < 0.1 %Below 100keV in air, the photoelectric effect becomes
            %dominant in iron. This loop kills low-energy
            %photons that interact in iron.

    if location <= nio     %This loop kills the track for low-energy
                    %interactions inside the near iron barrier.
        if location >= nii
            break
        end
    end

    if location <= fii     %This loop kills the track for low-energy
                    %interactions inside the far iron barrier.
        if location >= fio
            break
        end
    end
end




%Now we need the energy of the scattered photon. The Compton Formula
%provides this from the scattered angle.
energy=energy/(1+energy*(1-cos(scatterangle)));

if energy <.005     %This loop is an energy-based kill criteria for the track.
    break
end

%-------------------------------------------------------
```

%We cannot simply add the scattering angle to the angle of the photon.
%This is because a scattering angle is equally likely all around the axis
%of the incident photon. Thus, while we could simply add it to the zero
%angle of the initial photon, we cannot do so for further interactions.

%Since we are only interested in the projection of the scattered photon
%onto the axis of the plane of the slab, we can use the Law of Cosines for
%Spherical Triangles.

revolvingangle = 2*pi*rand(1);
angle = acos(cos(angle)*cos(scatterangle)+sin(angle)*sin(scatterangle)*cos(revolvingangle));

end

end

Spectrumdata=Energydata(Energydata~=0);

%Dosedata=zeros(1, (length(Spectrumdata))); %Initialize what will be an allocatable
        %array. This will track dose deposited in the detector volume.
%for m=1:length(Spectrumdata)
%   Dosedata(m)=(Spectrumdata(m)*(1.6*10^(-13))*NaAtten)+(Spectrumdata(m)*(1.6*10^(-13))*IAtten);
%end
%Dose=sum(Dosedata)
hist(Spectrumdata,662)

REPORT DOCUMENTATION PAGE				*Form Approved* *OMB No. 0704–0188*
The public reporting burden for this collection of information is estimated to average 1 hour per response, including the time for reviewing instructions, searching existing data sources, gathering and maintaining the data needed, and completing and reviewing the collection of information. Send comments regarding this burden estimate or any other aspect of this collection of information, including suggestions for reducing this burden to Department of Defense, Washington Headquarters Services, Directorate for Information Operations and Reports (0704–0188), 1215 Jefferson Davis Highway, Suite 1204, Arlington, VA 22202–4302. Respondents should be aware that notwithstanding any other provision of law, no person shall be subject to any penalty for failing to comply with a collection of information if it does not display a currently valid OMB control number. PLEASE DO NOT RETURN YOUR FORM TO THE ABOVE ADDRESS.				
1. REPORT DATE (DD–MM–YYYY) 26-03-2015	2. REPORT TYPE Master's Thesis		3. DATES COVERED (*From — To*) 28 June 2014 – 26 March 2015	
4. TITLE AND SUBTITLE Verification and validation of Monte Carlo N-Particle 6 for Computing Gamma Protection Factors			5a. CONTRACT NUMBER	
			5b. GRANT NUMBER	
			5c. PROGRAM ELEMENT NUMBER	
6. AUTHOR(S) Erwin, William J, Captain			5d. PROJECT NUMBER	
			5e. TASK NUMBER	
			5f. WORK UNIT NUMBER	
7. PERFORMING ORGANIZATION NAME(S) AND ADDRESS(ES) Air Force Institute of Technology Graduate School of 2950 Hobson Way WPAFB OH 45433-7765			8. PERFORMING ORGANIZATION REPORT NUMBER AFIT-ENP-MS-15-M-090	
9. SPONSORING / MONITORING AGENCY NAME(S) AND ADDRESS(ES) Defense Threat Reduction Agency Andrew W. Decker J9-NTW (NSERC), Defense Threat Reduction Agency (DTRA) West Point, NY 10996 andrew.decker@dtra.mil			10. SPONSOR/MONITOR'S ACRONYM(S) DTRA	
			11. SPONSOR/MONITOR'S REPORT NUMBER(S)	
12. DISTRIBUTION / AVAILABILITY STATEMENT Distribution Statement A. Approved for Public Release; Distribution Unlimited				
13. SUPPLEMENTARY NOTES This work is declared a work of the U.S. Government and is not subject to copyright protection in the United States.				
14. ABSTRACT This thesis examined the suitability of a particle simulator known as "Monte Carlo n-Particle 6 (MCNP6) to determine how well U.S. Army vehicles shield their occupants from gamma radiation. MCNP6 compared favorably to three alternate modeling approaches and another particle simulator. In a validation experiment, MCNP6 was found to produce a gamma protection factor within 5% of the experimental result with 95% confidence. Further evaluations validated MCNP6's ability to produce reliable results with simplified or approximated inputs, model different sources, and position those sources in different shielding geometries. MCNP6 is suitable for evaluating gamma protection of Army vehicles and further research to explore the effects of different shielding shapes and evaluate the suitability for MCNP6 to calculate a comprehensive radiation protection factor is warranted.				
15. SUBJECT TERMS Radiation, shielding, MCNP, protection factor				
16. SECURITY CLASSIFICATION OF:			17. LIMITATION OF ABSTRACT	18. NUMBER OF PAGES	19a. NAME OF RESPONSIBLE PERSON Dr. Justin A. Clinton ENP
a. REPORT U	b. ABSTRACT U	c. THIS PAGE U	UU	123	19b. TELEPHONE NUMBER (Include Area Code) (937) (937) 255-3636 x4586 justin.clinton.2@us.af.mil